The Astrophysical Journal, 972:172 (22pp), 2024 September 10 https://doi.org/10.3847/1538-4357/ad5d57

Retrieving Young Cloudy L Dwarfs: A Nearby Planetary-mass Companion BD+60 1417B and its Isolated Red Twin W0047

Caprice L. Phillips[1], Jacqueline K. Faherty[2], Ben Burningham[3], Johanna M. Vos[4], Eileen C. Gonzales[5,6,14], Emily J. Griffith[7,15], Sherelyn Alejandro Merchan[2,8], Emily Calamari[9,2], Channon Visscher[10,11], Caroline V. Morley[12], Niall Whiteford[2], Josefine Gaarn[3], Ilya Ilyin[13], Klaus Strassmeier[13], and Ji Wang[1]
[1] Department of Astronomy, The Ohio State University, 100 W 18th Avenue, Columbus, OH 43210, USA; phillips.1622@buckeyemail.osu.edu
[2] Department of Astrophysics, American Museum of Natural History, New York, NY 10024, USA
[3] Centre for Astrophysics Research, School of Physics, Astronomy and Mathematics, University of Hertfordshire, Hatfield, AL10 9AB, UK
[4] School of Physics, Trinity College Dublin, The University of Dublin, Dublin 2, Ireland
[5] Department of Physics and Astronomy, San Francisco State University, 1600 Holloway Avenue, San Francisco, CA 94132, USA
[6] Department of Astronomy and Carl Sagan Institute, Cornell University, 122 Sciences Drive, Ithaca, NY 14853, USA
[7] Center for Astrophysics and Space Astronomy, Department of Astrophysical and Planetary Sciences, University of Colorado, 389 UCB, Boulder, CO 80309-0389, USA
[8] Hunter College, City University of New York, 695 Park Avenue, New York, NY 10065, USA
[9] The Graduate Center, City University of New York, New York, NY 10016, USA
[10] Chemistry & Planetary Sciences, Dordt University, Sioux Center, IA 51250, USA
[11] Center for Extrasolar Planetary Systems, Space Science Institute, Boulder, CO 80301, USA
[12] Department of Astronomy, The University of Texas at Austin, Austin, TX 78712, USA
[13] Leibniz-Institut for Astrophysics Potsdam (AIP), An der Sternwarte 16, D-14482 Potsdam, Germany
Received 2024 April 26; revised 2024 June 14; accepted 2024 June 28; published 2024 September 5

Abstract

We present an atmospheric retrieval analysis on a set of young, cloudy, red L dwarfs—CWISER J124332.12+600126.2 (BD+60 1417B) and WISEP J004701.06+680352.1 (W0047)—using the Brewster retrieval framework. We also present the first elemental abundance measurements of the young K-dwarf (K0) host star, BD+60 1417, using high-resolution (R = 50,000) spectra taken with the Potsdam Echelle Polarimetric and Spectroscopic Instrument on the Large Binocular Telescope. In the complex cloudy L-dwarf regime the emergence of condensate cloud species complicates retrieval analysis when only near-infrared data are available. We find that for both L dwarfs in this work, despite testing three different thermal profile parameterizations we are unable to constrain reliable abundance measurements and thus the carbon-to-oxygen ratio. While we cannot conclude what the abundances are, we can conclude that the data strongly favor a cloud model over a cloudless model. We note that the difficulty in retrieval constraints persists regardless of the signal-to-noise ratio of the data examined (S/N $\sim$ 10 for CWISER BD+60 1417B and 40 for WISEP W0047). The results presented in this work provide valuable lessons about retrieving young, low-surface-gravity cloudy L dwarfs. This work provides continued evidence of missing information in models and the crucial need for JWST to guide and inform retrieval analysis in this regime.

Unified Astronomy Thesaurus concepts: Brown dwarfs (185); Atmospheric composition (2120); Substellar companion stars (1648); Fundamental parameters of stars (555); L dwarfs (894); Stellar abundances (1577)

1. Introduction

Brown dwarfs are a class of astronomical objects that are not massive enough (13–75 $M_{\rm Jup}$) to stably fuse hydrogen in their cores (Kumar 1963). As such, they contract and cool as they age and progress through spectral types (Kirkpatrick 2005). As the bridge between low-mass stars and directly imaged gas giants, brown dwarfs are key to understanding planetary atmospheres and planetary formation mechanisms (Faherty et al. 2016; Liu et al. 2016). Brown dwarfs that share the same parameter space (e.g., wide orbits/long orbital periods, colors, mass, radius, temperature, and spectral morphology) with directly imaged planets can be complementary to study (Burgasser 2010; Faherty et al. 2013a, 2013b, 2021). Furthermore, young, low-mass brown dwarfs are valuable laboratories for refining models of atmospheric chemistry and cloud formation. Studies have shown evidence for a correlation between clouds and youth (Faherty et al. 2013a, 2016; Vos et al. 2018). At younger ages (lower surface gravities), the sedimentation and appearance of clouds are affected, further highlighting the value of studying young, low-mass brown dwarfs (Marley et al. 2012; Suárez & Metchev 2022, 2023). As analogs of young directly imaged exoplanets they are ideal objects to test and verify models and atmospheric retrieval techniques. The direct detection and atmospheric studies of exoplanets remains a challenge due to the high contrast ratio with the host star (Marois et al. 2010; Chilcote et al. 2017; Rajan et al. 2017; Wang et al. 2020; Ruffio et al. 2021; Whiteford et al. 2023). Brown dwarfs can be studied in far greater detail than directly imaged exoplanets, as they are easier to observe. Overall, brown dwarfs have been used to inform our observational knowledge of extrasolar atmospheres and advance theoretical understanding of cool worlds (Burrows et al. 2011; Tremblin et al. 2017; Marley et al. 2021).

As far back as the discovery of the first methane-bearing brown dwarf, Gliese 229B (Nakajima et al. 1995;

[14] 51 Pegasi b Fellow.
[15] NSF Astronomy and Astrophysics Postdoctoral Fellow.

Oppenheimer et al. 1995), the exact formation mechanism for brown dwarfs has been debated. While they are largely thought to form like stars via cloud fragmentation, there are alternative pathways which might lead to the lowest-mass isolated sources (Bate et al. 2002; Whitworth & Goodwin 2005; Whitworth & Stamatellos 2006; Bonnell et al. 2008). Disk fragmentation and core accretion are two formation mechanisms that overlap with giant, widely separated exoplanets. Distinguishing between formation pathways has been tackled on the theoretical side (e.g., Luhman et al. 2007; Whitworth 2007, 2018; Whitworth et al. 2010) and recent space-based and ground-based data allow us to address it on the observational side with carbon-to-oxygen (C/O), [C/H], and [O/H] ratios (e.g., Madhusudhan et al. 2016; Maldonado & Villaver 2017; Gonzales et al. 2020, 2022; Burningham et al. 2021; Calamari et al. 2022; Vos et al. 2023).

C/O ratios may help inform what pathway of formation a given object followed, shedding light on whether brown dwarfs form in a disk like planets in our solar system or in a fragment of a molecular cloud like binary stars (Öberg et al. 2011). For example, at large orbital radii, we expect particularly strong differential evolution between gas and dust in the disk, which may translate to large observational differences in composition between substellar objects and their primary stars. Pertaining to planets, a stellar C/O ratio is expected for objects formed through gravitational instability, while superstellar C/O indicates accretion of solids. The C/O ratio of the companion can be compared to the host star to provide context for formation and evolution history. With spectroscopic observations of a host star, we can measure the star's photospheric abundances—a chemical fingerprint of the gas the system was born out of—and then have a base level for comparison to a companion (Konopacky et al. 2013; Wang et al. 2022; Hoch et al. 2023; Xuan et al. 2024).

Exoplanetary atmospheric retrieval (or the spectral retrieval method) refers to the inference of atmospheric properties of an exoplanet given an observed spectrum (Madhusudhan 2019). Using this method, one can retrieve the atmospheric abundances and in turn derive bulk abundances, which can be compared to their host-star values and to extract clues to their formation mechanisms (e.g., Wang et al. 2022, 2023; Xuan et al. 2022).

While a suite of retrieval frameworks have been developed in recent years (see review from MacDonald & Batalha 2023), for this work, we use the Brewster (Burningham et al. 2017) retrieval framework. Brewster is optimized for cloudy L dwarfs and was initially designed to model and capture the complexity in clouds in extrasolar atmospheres. Brewster has been utilized and tested on brown dwarfs in the L–T spectral-type regimes (e.g., Burningham et al. 2017, 2021; Gonzales et al. 2020, 2021, 2022; Calamari et al. 2022; Gaarn et al. 2023; Vos et al. 2023).

In this paper, we employ the Brewster spectral retrieval framework to understand the atmospheric structure and composition of two young red L dwarfs. In Section 2, we present literature data on both systems. In Section 3, we present spectroscopic data for CWISER J124332.12+600126.2 (hereinafter BD+60 1417B) and WISEP J004701.06+680352.1 (hereinafter W0047) along with newly obtained data for the host star BD+60 1417. In Section 4, we discuss the spectral energy distribution (SED) analysis used in the Brewster framework. We discuss the host-star parameters and abundance analysis in Section 5. In Section 6, we discuss the retrieval framework and modification settings used in our work. We present the retrieval analysis results for BD+60 1417B and W0047 in Sections 8 and 9, respectively. We provide key discussions in Section 10, and conclude in Section 11.

Table 1
Observed Properties and Derived Fundamental Parameters for BD +60 1417B and W0047

Property	BD+60 1417B	W0047	References
R.A.[a]	12:43:32.1025	00:47:00.3866	C03
Decl.[a]	+60:01:26.5150	+68:03:54.3672	C03
$\mu_\alpha \cos\delta$ (mas yr^{-1})	-133 ± 8	245.7 ± 5.4	M21, L16
μ_δ (mas yr^{-1})	-55 ± 8	-108.5 ± 2.4	M21, L16
Spectral type (IR)	L8γ	L7	F21, G15
Distance (pc)	44 ± 4	12.2 ± 0.4	F21, G15
Photometry			
Pan-STARRS y (mag)	20.481 ± 0.178	⋯	G21
2MASS J (mag)	>17.452	15.604 ± 0.068	C03
2MASS H (mag)	>16.745	13.968 ± 0.041	C03
2MASS K_S (mag)	13.582 ± 0.045	12.562 ± 0.024	C03
WISE W1 (mag)	14.594 ± 0.031	11.876 ± 0.023	C12
WISE W2 (mag)	13.872 ± 0.035	11.268 ± 0.020	C12
WISE W3 (mag)	⋯	10.327 ± 0.072	C13
Fundamental Parameters from SED Analysis			
$L_{\rm bol}$ ($L_{\rm bol}/L_\odot$)	-4.42 ± 0.10	-4.35 ± 0.06	TW
$T_{\rm eff}$ (K)	1240 ± 81	1291 ± 51	TW
Radius ($R_{\rm Jup}$)	1.29 ± 0.06	1.29 ± 0.03	TW
Mass ($M_{\rm Jup}$)	13.47 ± 5.67	15.65 ± 4.65	TW
$\log g$ (cm s^{-2})	4.26 ± 0.20	4.3 ± 0.1	TW

Note.
[a] Epoch J2000, ICRS.

References. F21: Faherty et al. (2021); TW: This Work; C03: Cutri et al. (2003); C12: Cutri et al. (2012); G15: Gizis et al. (2015); M21: Marocco et al. (2021); L16: Liu et al. (2016); G21: Gaia Collaboration et al. (2021).

2. Young Red L-dwarf Spectroscopic Twins: BD+60 1417B and W0047

The nearby (∼45 pc) recently discovered L6–L8γ companion, BD+60 1417B, is a planetary-mass ($15 \pm 5\ M_{\rm Jup}$) object prime for atmospheric characterization (Faherty et al. 2021). BD+60 1417B lies at a wide separation from its young (50–150 Myr) K0 host star (∼1662 au). Faherty et al. (2021) found that this object lies in a sparsely populated region of mass ratio versus separation parameter space, with only eight other objects, with an estimated mass $<20\ M_{\rm Jup}$ and an orbital separation >1000 au. BD+60 1417B has a mass ratio in line with known exoplanets but appears too widely separated to have formed as a planet in situ. Thus, there are open questions regarding its formation history and mechanism.

W0047 (Gizis et al. 2015) is an isolated red L7γ dwarf member of the ∼120 Myr AB Doradus moving group. Faherty et al. (2021) found that it was a spectroscopic twin to BD+60 1417B. BD+60 1417B and W0047 have similar masses, temperatures, and extremely red colors of $(J - K_s) = 2.72 \pm 0.34$ and $(J - K) = 2.55 \pm 0.2$, respectively (see Table 1). Additionally, both objects show signatures of condensate-cloud-driven variability (e.g., Vos et al. 2018; J. M. Vos et al. 2024, in preparation). Spitzer photometric monitoring was obtained for

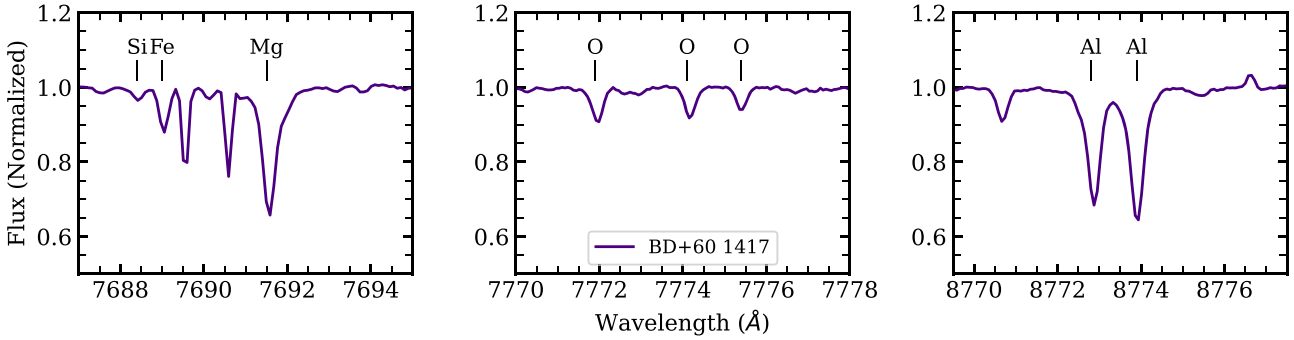

Figure 1. PEPSI spectra of BD+60 1417 in selected wavelength regions of 7687–7695 Å (left), 7770–7778 Å (center), and 8770–8777 Å (right). Line features used in the abundance analysis have been labeled.

W0047, which showed high amplitude variability of 1.07% ± 0.04%. This variability measurement put W0047 among the highest Spitzer variability amplitudes detected (Vos et al. 2018). These results are consistent with near-infrared variability amplitudes (11%) found for W0047 using the Hubble Space Telescope (HST; Lew et al. 2016). The similarities between W0047 and BD+60 1417B therefore drive our intercomparison of their resultant retrieved properties.

3. Data

3.1. Spectroscopic Data for BD+60 1417

BD+60 1417 is a nearby (∼45 pc; Gaia Collaboration et al. 2023) solar-type star (K0 spectral type). As summarized in Faherty et al. (2021), BD+60 1417 has numerous youth indicators, including a Li I abundance, measurement of a fast rotation rate, and a position on color–magnitude and color–color diagrams indicating youth, all of which point to an estimated age range of 50–150 Myr. However, until this paper, BD+60 1417 lacked a high-resolution spectrum used to calculate solar abundances. Therefore, we obtained high-resolution optical spectra of BD+60 1417 ($V = 9.364 \pm 0.11$) from the Potsdam Echelle Polarimetric and Spectroscopic Instrument (PEPSI; Strassmeier et al. 2015) on the Large Binocular Telescope (LBT) on 2023 February 9. Observations were taken with the 300 μm fiber for a resolution $R = \lambda/\Delta\lambda =$ 50,000 and with cross-dispersers (CDs) III and VI to obtain high-signal-to-noise ratio (S/N) spectra in the wavelength ranges 4800–5411 Å and 7419–9140 Å. This wavelength regime and resolution contains multiple stellar absorption features for C, O, Mg, Si, Ca, and Al. BD+60 1417 was observed for 1260 s, reaching a S/N of 795 in CD III and and 517 in CD VI. We plot selected regions of the spectra in Figure 1.

We employ the Spectroscopic Data System for PEPSI pipeline (SDS4PEPSI) to reduce the spectra of BD+60 1417, as described in Strassmeier et al. (2018). In short, this pipeline applies bias and flat-field corrections and estimates the photon-noise contribution to the spectra. It removes contamination from scattered light as well as cosmic rays. The pipeline conducts flux extraction and wavelength calibrates the spectra against Th–Ar lines, as well as corrects for the echelle's blaze function, fringing, and vignetting effects. Finally, the pipeline corrects for the star's radial velocity shifts to bring the spectra to rest-frame wavelengths and applies a continuum normalization by fitting a 2D smoothing spline in the cross-dispersion and dispersion directions.

3.2. Spectroscopic Data for BD+60 1417B and W0047

For BD+60 1417B, we use the published 1–2.5 μm Infrared Telescope Facility (IRTF)/SpeX Prism spectrum from Faherty et al. (2021) with $R \sim 100$ and S/N ∼ 9. The spectra for W0047 consist of a 1–2.5 μm IRTF/SpeX spectrum from Gizis et al. (2012) with $R \sim 150$ and S/N ∼ 37 and a 1.10–1.69 μm HST/WFC3 spectrum from Manjavacas et al. (2019) with $R \sim$ 130 and S/N ∼ 370 at 1.25 μm.

4. Fundamental Parameters from Spectral Energy Distributions for BD+60 1417B and W0047

In order to acquire fundamental parameters, we constructed and analyzed the SEDs for BD+60 1417B and W0047. We compiled all relevant data including the parallax measurements of BD+60 1417B and W0047 along with spectra and photometry to acquire a distance-calibrated SED. Wide-field Infrared Survey Explorer (WISE) W1 and W2 photometry was used from the catWISE2020 reject table, as BD+60 1417B was rejected from the main table because it was near a diffraction spike from the primary. We follow Faherty et al. (2021) and find the photometry to be usable for construction and analysis of the SED. We used the open-source package SEDkit (Filippazzo 2020) presented in Filippazzo et al. (2015) to construct the SED and derive the fundamental parameters of these twin analogs. Integrating under the flux-calibrated SED, we calculated the $L_{\rm bol}$ for each target. Pairing the $L_{\rm bol}$ values and ages of 100 ± 50 Myr (Faherty et al. 2021) and 120 ± 50 Myr (Gizis et al. 2015) for BD+60 1417B and W0047, respectively. Along with the Marley et al. (2021) evolutionary models, we semi-empirically calculate the $T_{\rm eff}$ and infer the radius, mass, and $\log g$. The SEDs of BD+60 1417B and W0047 are shown in Figure 2 and fundamental parameters derived from the SEDs are shown in Table 1.

The SED study and derived fundamental parameters for BD +60 1417B and W0047 emphasize the similar nature of these substellar objects, as indicated by their $T_{\rm eff}$ being within ∼50 K, identical radii, and mass measurements that extend into the nominal space between brown dwarfs and planets.

5. Spectral Parameter and Abundance Determination for BD+60 1417

5.1. Stellar Parameter Determination

We used the PEPSI reduced spectrum to determine stellar parameters and stellar abundances with MOOG, a LTE radiative transfer code (Sneden 1973), implemented through the iSpec wrapper (Blanco-Cuaresma et al. 2014; Blanco-Cuaresma 2019).

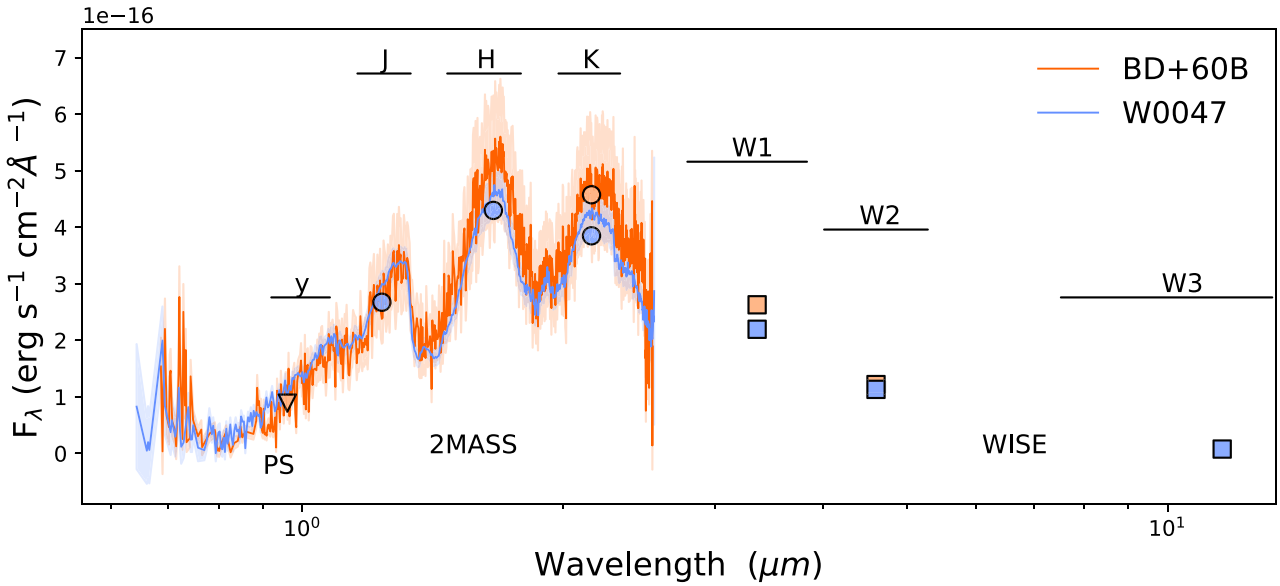

Figure 2. SEDs of BD+60 1417B and W0047. The distance-calibrated SEDs of BD+60 1417B and W0047 are shown in orange and blue, respectively. The SpeX/Prism spectrum for BD+60 1417B is shown in orange, with a shaded region indicating the flux uncertainties. Similarly, for W0047 the Spex/Prism and HST/WFC3 spectrum are shown in blue. Photometric points for W0047 are shown in a light blue and in light orange for BD+60 1417B. Circles are used for Two Micron All Sky Survey (2MASS), squares for WISE, and a downwards-pointing triangle for Pan-STARRS. The wavelength coverage for the photometric filters are indicated with horizontal lines. Error bars on the photometric points are smaller than the point size.

Stellar parameters $T_{\rm eff}$, $\log(g)$, [M/H], [α/M], and microturbulence velocity ($v_{\rm micro}$) are fit with equivalent-width analysis. Through iSpec, we fit the Fe I and Fe II lines in the Gaia-ESO version 6 line list (Gilmore et al. 2012; Heiter et al. 2021) with Gaussian or Voigt profiles and measure their equivalent widths. We remove the strongest and weakest lines by requiring that the reduced equivalent widths of the lines lie between −4.3 and −6.0 and by requiring that the lower-energy states of the lines lie between 0.5 and 5.0, as recommended by Mucciarelli et al. (2013), Blanco-Cuaresma et al. (2014), and Blanco-Cuaresma (2019). Using MARCS model atmospheres (Gustafsson et al. 2008) and Asplund et al. (2009) solar abundances, we implement MOOG equivalent-width parameter determination within iSpec, which iteratively fits models of $T_{\rm eff}$, $\log(g)$, [M/H], [α/M], and $v_{\rm micro}$, searching for a model that brings the Fe lines into ionization and excitation equilibrium. We initiate the parameter search at $T_{\rm eff} = 4993$ K, $\log(g) = 4.55$ dex, and [M/H] = 0.0 dex, based on the stellar parameters in the TESS input catalog (Stassun et al. 2018) adopted in Faherty et al. (2021). iSpec returns best-fit stellar parameters of $T_{\rm eff} = 5382 \pm 164$ K, $\log(g) = 4.88 \pm 0.06$ dex, [M/H] = 0.37 dex, [α/M] = 0.0 dex, and $v_{\rm micro} = 1.026$ km s^{-1}.

In addition to the above stellar parameters, MOOG and iSpec require values of macroturbulence ($v_{\rm macro}$), rotational velocity ($v \sin(i)$), spectral resolution (R), and limb-darkening coefficient to conduct stellar abundance determination with spectral synthesis. We set the resolution to that of the instrument (R = 50,000) and the limb-darkening coefficient to 0.6, as recommended by Blanco-Cuaresma et al. (2014). Because the broadening terms $v_{\rm macro}$ and $v \sin(i)$ are degenerate at R = 50,000, we set $v_{\rm macro} = 0$ km s^{-1} and find the best-fit $v \sin(i)$ through a spectral synthesis fit to the Fe I and Fe II line windows, with all other stellar parameters fixed to the values listed above Buder et al. (2021). We find that a $v \sin(i) = 5.40$ km s^{-1} best minimizes the residual between the synthetic and observed spectra.

To calculate the error on our stellar parameters, we run the equivalent width and spectral synthesis fits described above at the upper and lower bounds of $T_{\rm eff}$ to find the correlated deviations in $\log(g)$, [M/H], $v_{\rm micro}$, and $v \sin(i)$. We adopt an error of 0.12 dex on $\log(g)$, 0.04 dex on [M/H], 0.26 km s^{-1} on $v_{\rm micro}$, and 0.35 km s^{-1} on the broadening term $v \sin(i)$. We list all best-fit stellar parameters and their errors in Table 2.

We note that the photometric stellar parameters adopted as the initialization are not consistent with our calculated spectroscopic parameters. While the photometric $T_{\rm eff}$ and $\log(g)$ are derived from observables and used to calculate physical parameters such as stellar radii and mass, their adoption inhibits achieving ionization and excitation equilibrium in the Fe I and Fe II abundances. We adopt the spectroscopic parameters in further analysis as they are optimized for stellar abundance determination, but stress that these values should not be used to derive the stellar mass or radius (e.g., Jofré et al. 2019).

5.2. Stellar Abundance Determination

We determine the stellar abundances of C, O, Mg, Si, Ca, Al, and Fe with MOOG spectral synthesis implemented through iSpec. We use a curated line list created from referencing line lists from Fulbright (2000), GALAH Data Release 3 (Buder et al. 2021), and Gaia-ESO (Gilmore et al. 2012; Heiter et al. 2021), and the solar spectrum (Moore et al. 1966) comprised of five C I lines, three O I lines, 16 Mg I lines, 27 Si I lines, six Ca I lines, four Ca II lines, six Al I lines, 265 Fe I, and 10 Fe II lines. While the full spectrum was normalized in the SDS4PEPSI pipeline, we fit and normalize the continuum in the 8 Å region around each line window with a spline to ensure local continuum normalization.

For each element, we create windows of 5 Å around all relevant line features fit for the elemental abundance, with iSpec iteratively creating synthetic stellar spectra and finding the template with the abundance value that minimizes the

Table 2
Stellar Parameters and Abundances for BD+60 1417

Property	BD+60 1417
$T_{\rm eff}$	5381 ± 164 K
$\log(g)$	4.88 ± 0.12 dex
[M/H]	0.37 ± 0.04 dex
[α/M]	0.0 dex
$v \sin(i)$	5.40 ± 0.36 km s^{-1}
$v_{\rm micro}$	1.03 ± 0.26 km s^{-1}
[C/H]	-0.39 ± 0.14 dex
[O/H]	0.00 ± 0.18 dex
[O/H]$_{\rm NLTE}$	-0.02 ± 0.18 dex
[Mg/H]	0.13 ± 0.01 dex
[Si/H]	0.07 ± 0.06 dex
[Ca/H]	0.36 ± 0.02 dex
[Al/H]	0.15 ± 0.03 dex
[Fe/H]	0.27 ± 0.03 dex
C/O	0.23 ± 0.12
Mg/Si	1.41 ± 0.19
Ca/Al	1.26 ± 0.11

Notes. Unless noted, all [X/H] abundances are 1D LTE, relative to solar abundances in Asplund et al. (2009). We provide LTE and non-LTE (NLTE) [O/H] abundances. The reported C/O ratio is calculated from the NLTE [O/H] value.

residual between the synthetic and observed spectrum. We further fit each line of each element individually, finding consistent abundances between the lines of different ionization states for Si and Fe. We report the best-fit 1D LTE [C/H], [O/H], [Mg/H], [Si/H], [Ca/H], [Al/H], and [Fe/H] values in Table 2. We repeat the stellar abundance fits for each element with the upper and lower limits of the stellar parameters to calculate the abundance errors. The errors range from 0.01 dex (for Mg) to 0.18 dex (for O) and are also reported in Table 2.

In this paper, we calculate 1D LTE abundances for BD+60 1417. 3D and non-LTE (NLTE) effects are known to be a source of abundance uncertainty and can often cause abundance corrections >0.1 dex (e.g., Jofré et al. 2019). While we cannot integrate NLTE grids into iSpec, we use NLTE correction lookup tables from the Max Planck Institute for Astronomy to estimate the 1D NLTE corrections for O I (Bergemann et al. 2021), Mg I (Bergemann et al. 2017), Si I (Bergemann et al. 2013), Ca I, and Ca II (Mashonkina et al. 2007).[16] Tabulated NLTE corrections for C and Al are not yet available and are not accounted for in our reported errors. We find NLTE corrections of <0.01 dex for all available Mg and Si lines. While some Ca lines have significant NLTE corrections (−0.1 to 0.04 dex), the median value is <0.01 dex and does not impact our reported [Ca/H] abundance. The O triplet lines used in this analysis have a mean NLTE correction of −0.02 dex, leading to an NLTE [O/H] abundance of −0.02 dex.

From the [X/H] abundances, we can calculate the C/O, Mg/Si, and Ca/Al ratios. Each ratio represents the ratio of the number of atoms of element X to the number of atoms of element Y, where $\mathrm{X/Y} = N_{\rm X}/N_{\rm Y} = 10^{\log N_{\rm X}}/10^{\log N_{\rm Y}}$ and $\log N_{\rm X} = \log_{10}(N_{\rm X}/N_{\rm H}) + 12$. We calculate $\log N_{\rm X}$ as $[\mathrm{X/H}] + \log N_{\rm X,\odot}$, using solar abundances $\log N_{\rm X,\odot}$ of 8.43 for C, 8.69 for O, 7.60 for Mg, 7.51 for Si, 6.34 for Ca, and 6.45 for Al (Asplund et al. 2009). We report the resulting ratios in Table 2.

6. Brewster Framework for Retrieving BD+60 1417B and W0047

To extract comparative abundances for the brown dwarfs BD +60 1417B and W0047, we used the atmospheric retrieval code Brewster (Burningham et al. 2017). Below, we give a short description of the Brewster framework we utilized in this work. However, we encourage the reader to see a detailed description of Brewster in Burningham et al. (2017, 2021). Most notably, we differ from Burningham et al. (2017, 2021) with the use of a version update (Calamari et al. 2022) that utilizes nested sampling via `PyMultiNest` (Buchner et al. 2014) instead of `emcee`.

6.1. The Forward Model

The Brewster forward model uses the two-stream radiative transfer technique of Toon et al. (1989), including scattering, as first introduced by McKay et al. (1989) and subsequently used by Marley et al. (1996), Saumon & Marley (2008), and Morley et al. (2012). We set up a 64 pressure layer (65 levels) atmosphere with geometric mean pressures from $\log P = -4$ to 2.4 bars spaced in 0.1 dex intervals.

6.2. Thermal Profiles

A range of thermal profiles are used in retrieval analyses, ranging from a five-parameters joint exponential power law (Madhusudhan & Seager 2009; Burningham et al. 2017) to a 17-parameters free profile (Line et al. 2015). For this work, we aim to test a variety of thermal profiles for BD+60 1417B and W0047 to determine the reliability of retrieved abundances, pressure–temperature (P–T) profiles, bulk properties from ground-based near-infrared data, and the effect different thermal profile parameterizations have on retrieved abundances due to the notorious difficulty in modeling low-gravity objects (see thesis work by Niall Whiteford and GRAVITY Collaboration et al. 2020).[17] A similar exploration was conducted by Gonzales et al. (2022) and Rowland et al. (2023) for L dwarfs in a different regime.

In this work, we explore three different thermal profiles for our sources.

1. *Case 1: Five-point spline.* The initial thermal profile tested is a computationally simple five-point parameterization in which we specify five temperature–pressure points: the top ($T_{\rm top}$), bottom ($T_{\rm bottom}$), and middle of the atmosphere ($T_{\rm middle}$) and two midpoints between the top and middle ($T_{\rm q1}$) and bottom and middle ($T_{\rm q3}$). These points are calculated in order, beginning with $T_{\rm bottom}$, which is selected in a range between zero and the maximum temperature defined in our prior, which is 4000 K in this work. Then $T_{\rm top}$ is chosen between zero and $T_{\rm bottom}$, $T_{\rm middle}$ chosen between $T_{\rm top}$ and $T_{\rm bottom}$, and the remaining two midpoints chosen between $T_{\rm top}$ and $T_{\rm middle}$ ($T_{\rm q1}$) and $T_{\rm middle}$ and $T_{\rm bottom}$ ($T_{\rm q3}$). A uniform prior is assumed for each temperature within its respective range. This does not allow for temperature inversions but can result in "irregular" profiles.

[16] https://nlte.mpia.de/gui-siuAC_secE.php

[17] See https://era.ed.ac.uk/handle/1842/39547?show=full.

2. *Case 2: Lavie profile.* We introduce a second thermal profile parameterization developed and implemented by Lavie et al. (2017) in the HELIOS retrieval code and subsequently implemented into other retrieval frameworks (Whiteford et al. 2023). The Lavie profile is a less flexible profile with a simpler parameterization consisting of two free parameters, κ_0 and $T_{\rm int}$. The profile used in Lavie et al. (2017) originates from Heng et al. (2014), using a reduced form of Equation (126):

$$T^4 = \frac{T_{\rm int}^4}{4} \cdot \left(\frac{8}{3} + 3\tilde{m}\kappa_0\right), \quad (1)$$

where $T_{\rm int}$ is the internal temperature and κ_0 the constant component of the infrared opacity. $\tilde{m}$ is the column density, determined via $P_0 = \tilde{m} \cdot g$, where g is the surface gravity.

3. *Case 3: Mollière profile.* Lastly, we explore a modified version of the thermal profile parameterization implemented in Mollière et al. (2020; hereafter, the Mollière "Hybrid" profile). In the Mollière "Hybrid" profile, the atmosphere is split into three distinct regions: the photosphere (middle altitudes), high altitude, and troposphere (low altitudes). In the photosphere region, the temperature is set via an Eddington approximation:

$$T(\tau)^4 = \frac{3}{4}T_0^4\left(\frac{2}{3} + \tau\right), \quad (2)$$

where T_0 is a free parameter and $\tau = \delta P^{\alpha}$. For τ, δ and α are free parameters as well.

The high-altitude region is similar to that of Mollière et al. (2020). In the troposphere, our Mollière "Hybrid" profile differs from the implementation of Mollière et al. (2020), in that a dry adiabatic atmosphere (for H_2/He) is used instead of a moist adiabatic atmosphere. For a more detailed description of the Mollière "Hybrid" profile, we refer the reader to Mollière et al. (2020).

6.3. Gas Opacities

We consider the following absorbing gases in our analysis: H_2O, CO, CO_2, CH_4, CrH, FeH, Na, and K. These gases are chosen from Kirkpatrick (2005), as they have been previously identified as important absorbing species in the spectra of L6–L8 spectral types.

Optical depths due to absorbing gases for each layer are calculated using opacities sampled at a resolving power $R =$ 10,000 from the Freedman et al. (2008, 2014) collection with updated opacites from Burningham et al. (2017). Line opacites in our *P–T* range are tabulated in 0.5 dex steps for pressure and for temperature in steps ranging from 20 to 500 K as we move from 75 to 4000 K, which is then linearly interpolated to our working pressure grid.

We include continuum opacities for H_2–H_2 and H_2–He collisionally induced absorption, using cross sections from Richard et al. (2012) and Saumon et al. (2012), and include Rayleigh scattering due to H_2, He, and CH_4, but we neglect the remaining gases. Free–free continuum opacities are included for H^- and H_2^- as well as bound–free continuum opacity for H^- (Bell 1980; Bell & Berrington 1987; John 1988).

6.4. Determining Gas Abundances

We use the vertically constant mixing ratios method to determine gas abundances. The vertically constant method is sometimes referred to as a "free" retrieval method, which enables us to directly retrieve individual gas abundances under a computationally simple assumption of a single abundance for each gas throughout the 1D modeled atmosphere. It is considered "free" in the sense that there are no constraints imposed by thermochemical self-consistency. However, the simplicity of this method cannot capture important variations with altitude that are expected for some species, which can vary by several orders of magnitude in the photosphere (Rowland et al. 2023).

6.5. Cloud Model

We use the same simple cloud model utilized in previous works (e.g., Burningham et al. 2017; Gonzales et al. 2020, and Vos et al. 2023) where the cloud is parameterized as a "deck" or "slab." Both cloud types are defined where opacity due to the cloud is distributed among layers in pressure space and the optical depth defined as either gray or as a power law ($\tau = \tau_0\lambda^{\alpha}$, where τ_0 is the optical depth at 1 μm). As done in Gonzales et al. (2020), the single-scattering albedo is set to zero, thereby assuming an absorbing cloud.

The deck cloud is defined to always become optically thick at some pressure top, such that we only see the cloud top and the vertical extent of the cloud at pressures lower than $P_{\rm top}$. There are three parameters for the deck cloud: (1) a cloud-top pressure $P_{\rm top}$, the point at which the cloud passes $\tau = 1$ (looking down) for the first time ($P_{\rm deck}$); (2) the decay height $\Delta \log P$, over which the optical depth falls to lower pressures as $d\tau/dP \propto \exp((P - P_{\rm deck})/\Phi)$, where $\Phi = (P_{\rm top}(10^{\Delta \log P} - 1))/(10^{\Delta \log P})$; and (3) the cloud particle single-scattering albedo (α). At pressures $P > P_{\rm top}$, the optical depth increases following the decay function until $\Delta\tau_{\rm layer} = 100$. Deep below the cloud top there is essentially no atmospheric information as the deck cloud can rapidly become opaque with increasing pressure. Therefore, we stress that the *P–T* profile below the deck cloud top extends the gradient at the cloud-top pressure.

The slab cloud differs from the deck as it is possible to see the bottom of the slab. The slab parameters include deck parameters (1) and (3). Because it is possible to see to the bottom of the slab, parameter (2) is now a physical extent in log-pressure ($\Delta \log P$). We also include an additional parameter for determining the total optical depth of the slab at 1 μm ($\tau_{\rm cloud}$), bringing the total number of parameters to four. The optical depth is distributed through the slab's extent as $d\tau/dP \propto P$ (looking down), reaching its total value at the highest pressure (bottom) of the slab. The slab can have any optical depth in principle, however we restrict our prior as $0.0 \leqslant \tau_{\rm cloud} \leqslant 100.0$.

If the deck or slab cloud is nongray, an additional parameter for the power (α) in the optical depth is included.

7. Retrieval Model

The retrieval process consists of optimizing the parameters of the forward model such that the resultant spectrum provides the best match to the observed spectrum. As described by Burningham et al. (2017), we use a Bayesian framework to optimize the model fit to the data by varying the input parameters (Table 3). Following Calamari et al. (2022), we use

Table 3
Priors for BD+60 1417B and W0047 Retrieval Models

Parameter	Prior
Gas volume mixing ratio	Uniform, $\log f_{\rm gas} \geqslant -12.0$, $\sum_{\rm gas} f_{\rm gas} \leqslant 1.0$
Thermal profile ($T_{\rm bottom}$, $T_{\rm Top}$, $T_{\rm middle}$, $T_{\rm q1}$, $T_{\rm q3}$)	Uniform, 0 K $< T <$ 4000.0 K
Scale factor (R^2/D^2)	Uniform, 0.5 $R_{\rm Jup} \leqslant R \leqslant 2.5\ R_{\rm Jup}$
Gravity ($\log g$)	Uniform, 1 $M_{\rm Jup} \leqslant gR^2/G \leqslant 80\ M_{\rm Jup}$
Cloud top[a]	Uniform, $-4 \leqslant \log P_{\rm CT} \leqslant 2.3$
Cloud decay scale[b]	Uniform, $0 < \log \Delta\ P_{\rm decay} < 7$
Cloud thickness[c]	Uniform, $\log P_{\rm CT} \leqslant \log (P_{\rm CT} + \Delta P) \leqslant 2.3$
Cloud total optical depth at 1 μm	Uniform, $0.0 \leqslant \tau_{\rm cloud} \leqslant 80.0$
Single-scattering albedo (ω_0)	Uniform, $0.0 \leqslant \omega_0 \leqslant 1.0$
Wavelength shift	Uniform, $-0.01 < \Delta\lambda < 0.01$ μm
Tolerance factor	Uniform, $\log(0.01 \times \min(\sigma_i^2)) \leqslant b \leqslant \log (100 \times \max(\sigma_i^2))$

Notes.
[a] For the deck cloud this is the pressure where $\tau_{\rm cloud} = 1$; for a slab cloud this is the top of the slab.
[b] Decay height above the $\tau_{\rm cloud} = 1.0$ level only for deck cloud.
[c] Thickness and $\tau_{\rm cloud}$ only retrieved for slab cloud.

a modified sampler to the original version of Brewster that uses `PyMultinest` (Buchner et al. 2014) instead of `emcee` (Foreman-Mackey et al. 2013).

Brewster applies Bayes' theorem to calculate the "posterior probability," $p(\boldsymbol{x}|\boldsymbol{y})$, the probability of a set of parameters' ($\boldsymbol{x}$) truth value given some data ($\boldsymbol{y}$), in the following way:

$$p(\boldsymbol{x}|\boldsymbol{y}) = \frac{\mathscr{L}(\boldsymbol{x}|\boldsymbol{y})p(\boldsymbol{x})}{p(\boldsymbol{y})}, \tag{3}$$

where $\mathscr{L}(\boldsymbol{x}|\boldsymbol{y})$ is the likelihood that quantifies how well the data match the model, $p(\boldsymbol{x})$ is the prior probability on the parameter set, and $p(\boldsymbol{y})$ is the probability of the data marginalized over all parameter values, also known as the Bayesian evidence.

The posterior probability space is explored using the `PyMultiNest` sampler (Buchner et al. 2014), which utilizes nested sampling to discover the set of parameters with the maximum likelihood given the data. The samples in an n-dimensional hypercube, or state vector, are translated into parameter values via a "prior-map." The prior-map function is how prior probabilities are set for each parameter and are then transformed into appropriate parameter values to be used in the forward model. This algorithm is equipped to handle a parameter space that may contain multiple posterior modes and/or degeneracies in moderately high dimensions.

7.1. Model Selection

A variety of models were tested in our retrievals of BD+60 1417B and W0047. These models differed in their cloud prescriptions and P–T profile parameterizations, which are explained in Section 6. In order to compare all of our retrievals, we calculate the logarithm of the Bayesian evidence (log Ev), where the highest log Ev is preferred. For each of the models tested, the Δlog Ev is calculated by subtracting the log Ev of the winning model of the Bayesian evidence.

We use the following significance intervals from Kass & Raftery (1995) to distinguish between two models, with evidence against the lower log Ev as follows:

1. $0 < \Delta\log$ Ev < 0.5: no preference worth mentioning;
2. $0.5 < \Delta\log$ Ev < 1: positive;
3. $1 < \Delta\log$ Ev < 2: strong; and
4. $\Delta\log$ Ev > 2: very strong.

We began by building from the least complex model (cloud-free) to the most complex (power-law slab cloud model) for the three thermal profile parameterizations tested in this work for BD+60 1417B and W0047 (see Table 4).

8. BD+60 1417B Retrieval Results

We show the list of models tested for BD+60 1417B with the number of parameters and Δlog Ev for each model and thermal profile parameterization in Table 4.

8.1. Best-fit Models

The top-ranked model for BD+60 1417B was the power-law deck cloud model when using either the simple five-point spline or the Mollière "Hybrid" thermal profile. When using the Lavie thermal profile, the gray deck cloud model was top ranked and the power-law deck cloud was a close third. With Δlog Ev greater than 2 in all three cases, it is clear that the cloudless model is strongly rejected, indicating that the data strongly favor a cloud model to fit the spectroscopic features observed in BD+60 1417B.

8.2. Thermal Profiles

We show the retrieved thermal profiles and cloud pressures for the winning models compared to Sonora Diamondback self-consistent grid models (Morley et al. 2024) and condensation curves for BD+60 1417B in Figure 3. For the grid models shown, the base model has a $T_{\rm eff} = 1300$ K, $\log g = 4.5$, and a sedimentary efficiency $f_{\rm sed} = 1$–3. These values are selected from the SED-derived parameters for BD+60 1417B.

For the five-point spline profile (Figure 3(a)) there exists a slight thermal inversion near the top of the atmosphere, which we conclude is unphysical. This phenomenon is a byproduct of the five-point "irregular" thermal profile (Calamari et al. 2022). Additionally, we note that the retrieved thermal profile is not in agreement with the Sonora Diamondback grid models at the predicted temperature, especially within the photosphere (indicated by light gray shading), where our retrieved profile exhibits primarily warmer temperatures than the models predict. In the bottom half of the observable photosphere, our retrieved profile is nearly isothermal. Near the top of the visible photosphere region, the $f_{\rm sed} = 1$ model is near the same temperature as our retrieved profile. The location of the median cloud deck (1σ) is within the observable photosphere for the five-point thermal parameterization. Generally, we find that the best-fit retrieval using the five-point spline thermal profile for BD+60 1417B looks physically implausible (Figure 3(a)).

Figure 3(b) shows the retrieved thermal profile for the winning model for the Lavie thermal profile. The Lavie profile is a less flexible profile, which forces an almost isothermal profile above the photosphere. In the photosphere region, the thermal profile for BD+60 1417B is cooler than Sonora Diamondback grid models' predictions. The cloud top is near the bottom of the photosphere.

Table 4
List of Models and Thermal Profiles Tested in This Work for BD+60 1417B and W0047 along with the Corresponding Δlog Ev

Models	*N* Parameters	BD+60 1417B	W0047	BD+60 1417B	W0047
Five-point *P–T* Parameterization		Δlog Ev	Δlog Ev	log Ev	log Ev
Cloudless	16	−21.3	−4.52E+03	7.767E+03	5.159E+03
Gray deck cloud	18	−0.7	−19.75	7.787E+03	9.660E+03
Gray slab cloud	19	−9.5	−22.82	7.778E+03	9.657E+03
Power-law deck cloud	19	0.0	0.00	7.788E+03	9.680E+03
Power-law slab cloud	20	−5.9	−11.62	7.782E+03	9.668E+03
Lavie Profile					
Cloudless	13	−69.3	−176.66	7.702E+03	9.463E+03
Gray deck cloud	15	0.0	−74.75	7.772E+03	9.565E+03
Gray slab cloud	16	−5.59	−80.7	7.767E+03	9.559E+03
Power-law deck cloud	16	−6.5	0.00	7.766E+03	9.640E+03
Power-law slab cloud	17	−12.37	−71.26	7.760E+03	9.568E+03
Mollière "Hybrid" Profile					
Cloudless	17	−36.18	−180.36	7.751E+03	9.505E+03
Gray deck cloud	19	−2.13	−60.36	7.785E+03	9.622E+03
Gray slab cloud	20	−10.97	−95.00	7.776E+03	9.588E+03
Power-law deck cloud	20	0.00	0.00	7.778E+03	9.683E+03
Power-law slab cloud	21	−11.81	−18.19	7.775E+03	9.664E+03

Note. The lowest Δlog Ev (e.g., 0.0) corresponds to the "winning" model for each respective thermal parameterization for BD+60 1417B and W0047.

In Figure 3(c), we show the retrieved thermal profile and cloud pressure for the winning model for BD+60 1417B for the Mollière thermal parameterization. In the photosphere region, the retrieved profile is nearly isothermal and the median cloud lies within the observable photosphere, similar to the five-point spline model. In the regions extrapolated below the observable photosphere, the $f_{\rm sed} = 2$ and $f_{\rm sed} = 3$ models most closely trace the extrapolated profile.

8.3. Contribution Functions and Retrieved Spectra

The contribution function in a layer is defined as

$$C(\lambda, P) = \frac{B(\lambda, T(P)) \int_{P_1}^{P_2} d\tau}{\exp \int_0^{P_2} d\tau}, \quad (4)$$

where $B(\lambda, T(P))$ is the Planck function, zero is the pressure at the top of the atmosphere, P_1 is the pressure at the top of the layer, and P_2 is the pressure at the bottom of the layer. The contribution function indicates the location in the atmosphere where observable emission features are produced from and where spectral features become muted. The $\tau = 1$ gas and cloud contribution for winning models are shown as well.

Figure 4(a) shows the contribution function for the five-point spline thermal profile model for BD+60 1417B for the winning model of the power-law cloud deck. The $\tau = 1$ gas and cloud contributions are shown. The majority of the flux contribution to the observed spectrum comes from an approximately 0.004 to 2 bar region, corresponding to the photosphere. The *K* band is shaped by the cloud opacity, which has a more significant contribution. In the *J* and *H* bands, the gas opacity contributes more, which are the wavelength regions corresponding to H_2O molecular band features. There are windows in the *J* (≈1.2–1.4 μm) and *H* (≈1.6–1.8 μm) bands where the cloud opacity dominates.

Figure 4(b) shows the contribution function for the Lavie thermal profile for BD+60 1417B for the winning model, the power-law cloud deck. The bulk of the flux between ≈0.7 and 20 bars contributes to the observed spectrum. Across the spectrum, the cloud opacity becomes more important, with the exception of a small region in the *H* band (≈1.8–2.0 μm), where the gas opacity dominates.

Figure 4(c) shows the contribution function for the Mollière "Hybrid" thermal profile. The contribution function is similar to the five-point spline thermal profile. One of the key differences is the dominance of the cloud opacity in the entire *J*-band region. Between 1.3 and 1.5 μm is the only region where the gas opacity has a larger contribution.

We show all the retrieved spectra for BD+60 1417B in Figure 5 for our winning fits. The retrieved forward-model spectra consist of both the maximum-likelihood spectrum and median spectrum. The maximum-likelihood spectrum is the spectrum that maximizes the likelihood (i.e., the best fit from every single iteration). In the retrieval, the median spectrum is the spectrum from the median value of each retrieved parameter which is put into the forward model. Utilizing both the maximum-likelihood and the median spectra explores the parameter space well, and ideally these two retrieved fits should be near identical.

Figure 5(a) shows the retrieved spectrum for BD+60 1417B for the five-point spline thermal profile. The retrieved spectrum shows good agreement through the *J* and *H* spectral bands. However, the retrieved spectrum shows a worse fit in the *K* band, which holds the temperature-dependent CO molecular bands. The retrieved spectrum appears too

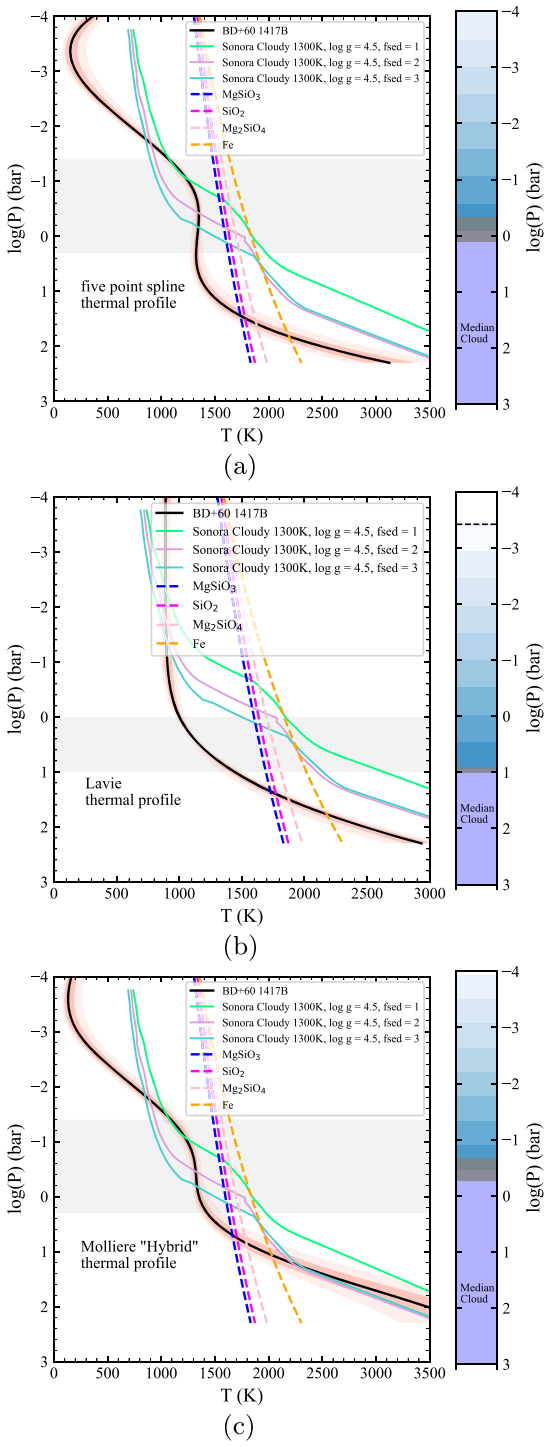

Figure 3. Retrieved thermal profile (black line, light red shading for 1σ and 2σ intervals) and cloud pressure for BD+60 1417B of the winning models for tested thermal profiles. Dashed lines show the condensation curves for possible cloud species. The light gray region is the approximate photosphere. Self-consistent grid models from Sonora Diamondback (Morley et al. 2024) for SED-derived temperature are plotted as solid colored lines. The median pressures of the extent of the cloud is shown in purple shading, with gray shading indicating the 1σ range, and blue shading showing the vertical distribution of the deck cloud over which the optical depth drops to 0.5. (a) BD +60 1417B retrieved thermal profiles for five-point spline, (b) Lavie profile (c) Mollière "Hybrid" profile.

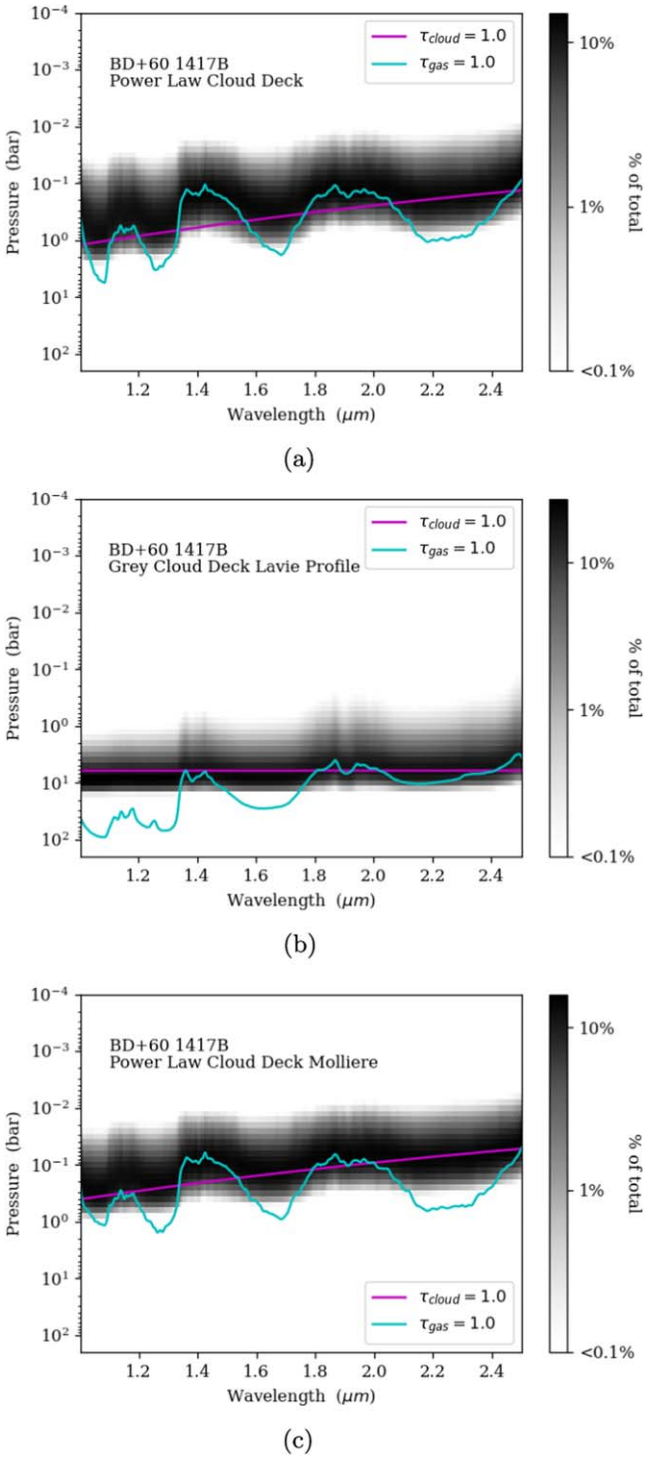

Figure 4. Contribution functions for BD+60 1417B based on the top-ranked model for each thermal parameterization case. The black shading shows the percentage contribution of each pressure to the flux at each wavelength. $\tau = 1$ lines are included for gas-phase opacities (cyan), and a cloud (magenta). (a) BD +60 1417B contribution function for five-point spline thermal profile, (b) Lavie profile, (c) Mollière "Hybrid" profile.

faint for the K band overall, which may explain our poorly constrained CO abundance in the five-point spline thermal parameterization.

Figure 5(b) shows the retrieved spectrum for the Lavie profile for BD+60 1417B. We note that the retrieved spectrum is fainter than the flux peaks in the H spectral band, which contains the gravity-sensitive triangular-band shape; this is in contrast to the five-point spline thermal profile. Similarly, the K spectral band is poorly fit as well.

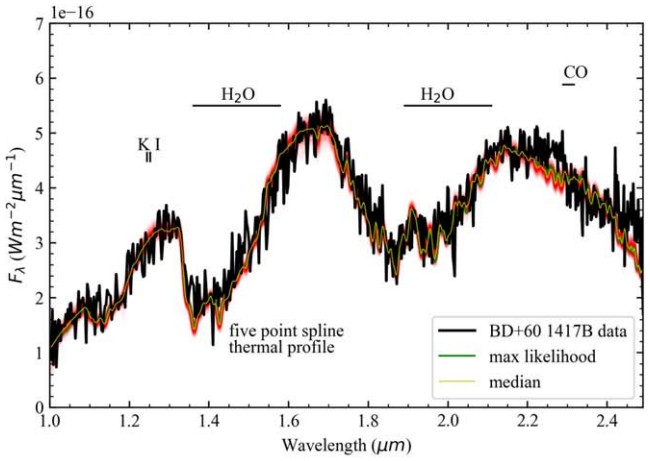

(a)

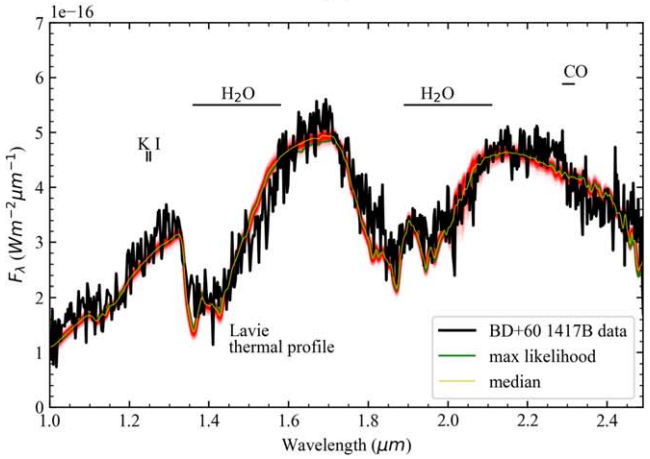

(b)

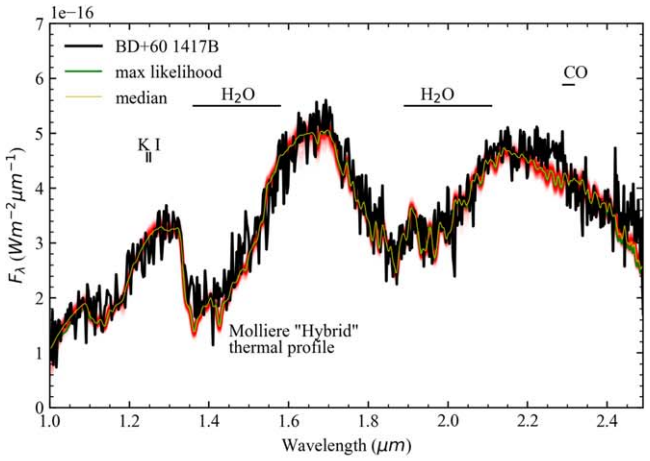

(c)

Figure 5. Retrieved forward-model spectra for BD+60 1417B. The maximum-likelihood spectrum is shown in green and the median spectrum in yellow. The SpeX prism data are shown in black. (a) BD+60 1417B retrieved spectra for five-point spline thermal profile, (b) Lavie profile, (c) Mollière "Hybrid" profile.

Figure 5(c) shows the retrieved spectrum for the Mollière thermal profile for BD+60 1417B. Similar to the Lavie retrieved profile (Figure 5(b)), the *K* band is too faint, which contains the CO band-head features.

8.4. Retrieved Gas Abundances and Fundamental Parameters

Figure B1 shows the posterior distributions for the radius, mass, metallicity, C/O, and $T_{\rm eff}$ for the retrieval case of BD +60 1417B. The derived log(g) is calculated from the retrieved radius and mass. The scale factor (R^2/D^2) is calculated from the retrieved radius and parallax. $T_{\rm eff}$ is then determined using this derived scale factor and by integrating the flux in the resultant forward-model spectra extrapolated to cover 0.5–20 μm.

Determining the C/O ratios of substellar objects involves retrieving the following abundances (X):

$$\frac{\rm C}{\rm O} = \frac{X_{\rm CO} + X_{\rm CO_2} + X_{\rm CH_4}}{X_{\rm CO} + 2X_{\rm CO_2} + X_{\rm H_2O}}. \quad (5)$$

Given our limited spectral coverage and retrieved abundances, when appropriate the C/O ratio is calculated under the assumption that all of the oxygen exists in H_2O and CO and all of the carbon exists in CO. Our ratio is considered as a CO-to-H_2O ratio. We note, however, that broader wavelength range retrievals for L dwarfs (e.g., Burningham et al. 2021) suggest that CO_2 abundances are higher than expected, and may need to be taken into account for this total ratio:

$$\frac{\rm C}{\rm O} = \frac{X_{\rm CO}}{X_{\rm CO} + X_{\rm H_2O}}. \quad (6)$$

The following equations were used to derive a value for metallicity, [M/H]:

$$f_{\rm H_2} = 0.84(1 - f_{\rm gas}), \quad (7a)$$

$$N_{\rm H} = 2f_{\rm H_2} N_{\rm tot}, \quad (7b)$$

$$N_{\rm element} = \sum_{\rm molecules} n_{\rm atom} f_{\rm molecule} N_{\rm tot}, \quad (7c)$$

$$N_{\rm M} = \sum_{\rm element} \frac{N_{\rm element}}{N_{\rm H}}, \quad (7d)$$

where $f_{\rm H_2}$ is the H_2 fraction, $f_{\rm gas}$ is the total gas fraction for all other gases, 0.84 represents the fraction of gas that is H_2, $N_{\rm H}$ is the number of neutral hydrogen atoms, $N_{\rm element}$ is the number of atoms for each element of interest, $n_{\rm atom}$ is the number of atoms for a given element contained in a single molecule, and $N_{\rm tot}$ is the total number of gas molecules.

In our calculation of metallicity, $N_{\rm solar}$ is determined using the same formula as $N_{\rm M}$, using the sum of the solar abundances (from Asplund et al. 2009) relative to H:

$$[{\rm M/H}] = \log \frac{N_{\rm M}}{N_{\odot}}. \quad (8)$$

In Table 5, we show the retrieved gas abundances for the winning models for the three thermal profile parameterizations for BD+60 1417B and W0047.

Figure 6 shows the retrieved gas mixing ratios compared to predictions from thermochemical equilibrium models. The thermochemical equilibrium models are calculated and interpolated for our derived metallicity and C/O ratio for the three thermal profile parameterizations for BD+60 1417B where applicable. In the cases where the C/O ratio and [M/H] are unable to be determined (due to nonphysical results), we assume solar values (Asplund et al. 2009); this is the case for the five-point spline profile and the Mollière "Hybrid" profile.

In Figure 6(a), for the five-point spline thermal profile major atmospheric constituents (CO and H_2O) in the photosphere

Table 5
Comparison of Retrieved Gas Abundances for the Preferred Models for BD +60 1417B and W0047 for Our Various Thermal Profile Parameterizations

	BD+60 1417B	W0047
Five-point Profile		
H_2O	$-0.40^{+0.21}_{-0.27}$	$-0.68^{+0.22}_{-0.20}$
CO	$-7.38^{+3.00}_{-2.83}$	$-8.96^{+2.44}_{-1.69}$
CO_2	$-5.73^{+2.60}_{-3.13}$	$-6.68^{+2.32}_{-2.74}$
CH_4	$-8.16^{+2.44}_{-2.37}$	$-7.60^{+3.35}_{-2.34}$
CrH	$-8.05^{+2.44}_{-2.37}$	$-5.90^{+0.27}_{-0.31}$
FeH	$-9.07^{+1.98}_{-1.96}$	$-8.67^{+1.34}_{-1.70}$
Na+K	$-7.90^{+3.30}_{-2.64}$	$-8.45^{+2.46}_{-1.92}$
Lavie Profile		
H_2O	$-3.34^{+0.05}_{-0.05}$	$-1.48^{+0.12}_{-0.06}$
CO	$-8.15^{+2.46}_{-2.10}$	$-1.76^{+0.21}_{-0.39}$
CO_2	$-5.78^{+2.46}_{-3.97}$	$-4.13^{+0.78}_{-0.97}$
CH_4	$-8.31^{+1.78}_{-1.96}$	$-3.10^{+0.19}_{-0.23}$
CrH	$-9.39^{+1.00}_{-1.39}$	$-10.94^{+0.48}_{-0.35}$
FeH	$-10.07^{+0.85}_{-0.98}$	$-10.56^{+0.67}_{-0.50}$
Na+K	$-8.58^{+2.15}_{-1.94}$	$-2.32^{+0.18}_{-0.15}$
Mollière "Hybrid" Profile		
H_2O	$-0.44^{+0.23}_{-0.29}$	$-0.58^{+0.24}_{-0.38}$
CO	$-6.75^{+2.96}_{-2.99}$	$-1.78^{+0.58}_{-5.55}$
CO_2	$-6.60^{+3.26}_{-3.01}$	$-7.64^{+2.39}_{-2.23}$
CH_4	$-8.07^{+2.30}_{-2.16}$	$-8.32^{+2.59}_{-2.07}$
CrH	$-7.33^{+1.80}_{-2.57}$	$-8.58^{+2.47}_{-2.38}$
FeH	$-8.27^{+1.50}_{-1.91}$	$-6.69^{+0.43}_{-0.80}$
Na+K	$-6.69^{+3.19}_{-3.05}$	$-8.59^{+3.00}_{-1.95}$

denoted by the gray box, we see that the gases are not predicted to vary greatly with altitude for our assumed solar abundances. However, our retrieved abundance for H_2O is implausibly high and does not match thermochemical equilibrium predictions. For the FeH abundance, our uniform with altitude abundance is in disagreement with the model thermochemical abundance predictions, which are predicted to vary with altitude in the photospheric region. Conversely, we see that while the Na+K abundance is uniform with altitude in the atmospheres, our median retrieved abundance is depleted compared to the equilibrium predictions. Additionally, we see that our CO measurement for the five-point spline thermal profile shows a depletion compared to predictions. This depletion could be the result of poor fits to the *K*-band region of the spectrum for BD +60 1417B as shown in Figure 5(a).

In Figure 6(b), we show our retrieved gas mixing ratios along with predictions from thermochemical equilibrium models interpolated for our derived metallicity and C/O ratio for the Lavie thermal profile. For H_2O, we see a slight disagreement ($>1\sigma$) in the photospheric region for our retrieved abundance in comparison to the thermochemical equilibrium models. Similar to the five-point spline profile, we observe a depletion of predicted CO in the photosphere region that might be due to the poor fits in the *K*-band region. The CO is also predicted to vary with altitude in the photosphere, which cannot be accounted for in our uniform with altitude abundance retrieval model. The retrieved FeH abundance shows photospheric agreement near the 10 bar region. While an overall poor constraint, for the CO_2 retrieved abundances we see an agreement with the predicted abundance that is within the 1σ error bar. The Na+K retrieved abundances are depleted compared to thermochemical equilibrium models.

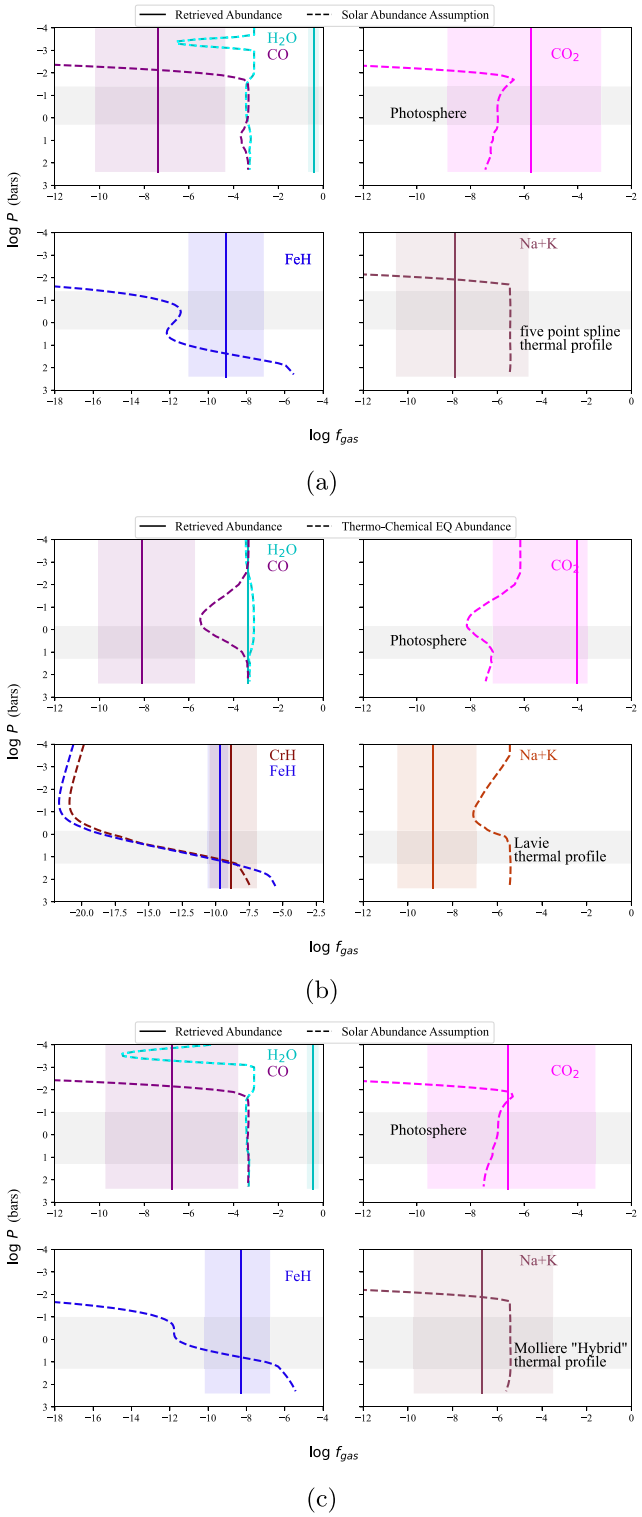

Figure 6. Retrieved uniform with altitude mixing abundances (solid lines) compared to thermochemical equilibrium grid abundances (dashed lines) for BD+60 1417B. Equilibrium predictions are calculated for assumed solar abundance or calculated based on derived [M/H] and C/O values. Shaded regions around the retrieved abundance values show our median retrieved values and 16th to 84th percentiles, respectively. Mixing abundances for the (a) five-point spline profile, (b) Lavie profile, (c) Mollière "Hybrid" profile.

Table 6
Comparison of Fundamental and Derived Parameters for the BD+60 1417B and W0047 Winning Models for Each Thermal Profile Parameterization

BD+60 1417B				
	Five Point	Lavie	Mollière	SED[a]
Radius ($R_{\rm Jup}$)	$0.59^{+0.10}_{-0.06}$	0.51 ± 0.01	$0.75^{+0.11}_{-0.08}$	1.29 ± 0.06
Mass ($M_{\rm Jup}$)	$40.83^{+10.47}_{-9.50}$	$61.11^{+9.53}_{-10.96}$	$36.54^{+13.94}_{-12.61}$	13.47 ± 5.67
log g (cm s^{-2})	$5.45^{+0.11}_{-0.15}$	$5.76^{+0.061}_{-0.09}$	$5.20^{+0.16}_{-0.19}$	4.26 ± 0.20
$T_{\rm eff}$ (K)	$826.35^{+42.10}_{-63.09}$	$889.47^{+7.19}_{-8.64}$	$735.20^{+45.62}_{-50.67}$	1240 ± 81
log ($L_{\rm bol}/L_{\rm Sun}$)	-5.81 ± 0.01	-5.81 ± 0.00	-5.81 ± 0.01	-4.42 ± 0.10
C/O	…	$0.02^{+0.24}_{-0.02}$	…	…
[M/H]	$2.71^{+0.45}_{-0.38}$	$-0.38^{+0.35}_{-0.10}$	$2.67^{+0.48}_{-0.40}$	…
W0047				
Radius ($R_{\rm Jup}$)	0.51 ± 0.01	0.51 ± 0.01	0.51 ± 0.01	1.29 ± 0.03
Mass ($M_{\rm Jup}$)	$50.28^{+11.22}_{-10.43}$	$59.54^{+6.24}_{-3.29}$	$45.45^{+15.63}_{-23.39}$	15.65 ± 4.65
log g (cm s^{-2})	$5.68^{+0.09}_{-0.10}$	$5.75^{+0.04}_{-0.03}$	$5.63^{+0.13}_{-0.30}$	4.3 ± 0.1
$T_{\rm eff}$ (K)	$872.35^{+6.90}_{-9.01}$	$875.86^{+6.48}_{-7.56}$	$871.47^{+7.31}_{-10.44}$	1291 ± 51
log ($L_{\rm bol}/L_{\rm Sun}$)	-5.84 ± 0.00	-5.84 ± 0.00	-5.84 ± 0.00	-4.35 ± 0.06
C/O	…	$0.35^{+0.12}_{-0.14}$	$0.05^{+0.28}_{-0.05}$	…
[M/H]	$2.32^{+0.30}_{-0.24}$	$1.80^{+0.13}_{-0.14}$	$2.55^{+0.31}_{-0.30}$	…

Note.
[a] Values are from the fundamental parameters derived from SED analysis (see Section 4).

For the Mollière thermal profile, similar to the five-point spine thermal profile, for the major atmospheric constituents (CO and H_2O) in the photosphere, we see that the gases are not predicted to vary greatly with altitude for our assumed solar abundances. We again see an implausibly high retrieved H_2O abundance. For FeH, our retrieved abundance is consistent with the predicted abundance at the bottom of the photosphere at 10 bar. The Na+K retrieved abundance is not predicted to vary with altitude and the values for the thermochemical equilibrium models are within the 1σ ranges for our retrieved values.

Table 6 shows a comparison of the fundamental and derived parameters for BD+60 1417B and the analog object W0047 for the three different thermal profile parameterizations. We find that for all three of our thermal parameterization checks for BD +60 1417B our fundamental parameters are in disagreement with the SED parameters. We discuss this in more detail in Section 10.3.

8.5. Cloud Properties

We find that the spectrum for BD+60 1417B is best described by a cloudy model regardless of thermal profile parameterization. This remains our strongest retrieval conclusion in the absence of being able to definitively converge on either a *P–T* profile or reasonable chemical abundances. A summary of cloud parameters for BD+60 1417B is shown in Table 7. We note a positive slope in the contribution function for the five-point spline thermal profile, which can be indicative of large particles (1 μm) in the atmosphere from Mie theory (e.g., Lacy & Burrows 2020). Where appropriate, the α parameter is positive for the power law.

The pressure of the cloud in the atmosphere of BD+60 1417B is shown in various shaded regions to the right of Figure 3. The notable difference is that the pressure at which $\tau > 1$ for the Lavie profile is higher than those for the five-point spline and Mollière "Hybrid" thermal profile. For BD+60 1417B the cloud height is similar for the five-point spline and Lavie profile, while the Mollière "Hybrid" profile cloud location extends further in the photosphere.

Table 7
Summary of Retrieved Cloud Properties for the Preferred Models of Respective Thermal Parameterization for BD+60 1417B and W0047

BD+60 1417B			
Thermal profiles	Five-point *P–T* profile	Lavie profile	Mollière "Hybrid" profile
Preferred cloud type	Power-law deck cloud	Gray deck cloud	Power-law deck cloud
PdeckC1P1 (bar)	$-0.08^{+0.19}_{-0.25}$	$0.95^{+0.06}_{-0.05}$	$-0.46^{+0.19}_{-0.21}$
Height/$d \log P$ (bar)	$4.39^{+1.49}_{-1.94}$	$4.37^{+1.39}_{-1.56}$	$3.91^{+1.59}_{-1.60}$
PowC1P1 α	$2.86^{+0.33}_{-0.37}$	n/a	$2.58^{+0.29}_{-0.28}$
W0047	Power-law deck cloud	Power-law deck cloud	Power-law deck cloud
PdeckC1P1 (bar)	$-0.17^{+0.07}_{-0.08}$	$0.09^{+0.05}_{-0.08}$	$-0.23^{+0.07}_{-0.08}$
Height/$d \log P$ (bar)	$3.34^{+1.58}_{-1.20}$	$4.97^{+0.55}_{-0.42}$	$4.85^{+1.12}_{-1.46}$
PowC1P1 (α)	$2.43^{+0.14}_{-0.14}$	$1.55^{+0.05}_{-0.07}$	$2.30^{+0.14}_{-0.15}$

9. W0047 Retrieval Results: A Comparative Example

The original aim of this work was to use retrieval analysis and the Brewster framework to understand the newly discovered young, low-surface-gravity, planetary-mass companion BD+60 1417B. However, we found that despite testing three different thermal parameterizations from the literature, often times not only did our fundamental parameters not match the SED analysis but we arrived at implausibly high or unconstrained molecular abundances for this benchmark object.

In Faherty et al. (2021), the isolated L dwarf W0047 was found to be a close match in spectral morphology and fundamental characteristics to BD+60 1417B (Table 1).

W0047 is an isolated object with higher-S/N SpeX prism observations (S/N $\sim$ 5 versus S/N $\sim$ 13) than BD+60 1417B, and slightly brighter apparent magnitude. We aim to use the same retrieval framework on this isolated, clone object to see if more robust results are obtained on higher-quality data. Table 4 shows the list of models tested for W0047, along with the number of parameters for each model and the resulting Δlog Ev.

9.1. Best-fit Models

The power-law deck cloud is preferred by all three thermal parametrizations tested. For this comparable object to BD+60 1417B, it is again evident that, based on our selection criterion, cloudless models are strongly rejected for all three different thermal parameterizations. Once again, this emphasizes our strongest retrieval conclusions: W0047 is a cloudy L dwarf. W0047 is known to be variable in the infrared, likely driven by nonuniform condensate clouds (Lew et al. 2016; Vos et al. 2018), thus our retrieval conclusion is not unexpected.

9.2. Thermal Profiles

Figure 7 shows the retrieved thermal profiles and cloud pressures for the winning models compared to grid models and condensation curves for W0047. For the five-point spline (Figure 7(a)), the retrieved thermal profile is not in agreement with the grid models, as was seen for BD+60 1417B. In the photosphere, the retrieved thermal profile is $\sim$300–400 K warmer than the grid models. The shape of the retrieved thermal profile is nearly linear throughout the photosphere and the extrapolated regions above and below the photosphere. The grid model that has the closest fit to the retrieved thermal profile in the photosphere is the $f_{\rm sed} = 1$ model. The median cloud location 1σ range is within the photosphere.

For the Lavie thermal profile parameterization (Figure 7(b)), we find that the retrieved thermal profile is not well aligned with the grid models. The cloud is located within the observable photosphere. Below the observable photosphere, the closest fitting model is $f_{\rm sed} = 1$.

Figure 7(c) shows the retrieved thermal profile for the Mollière thermal parameterization. The models ($f_{\rm sed} = 1$–3) are generally not in agreement with the retrieved profile in the photosphere region. Above the photosphere in the extrapolated region, the models diverge more from the extrapolated thermal profile. For the Mollière profile, the cloud deck is prevalent within the photosphere.

9.3. Contribution Functions and Retrieved Spectra

For the retrieved spectra for W0047 (Figure 8(a)), the five-point spline approach underestimates the flux in the *H*- and *K*-band peaks, hence the CO bands ($\approx$2.2–2.4 μm) are not fit well. This is a similar conclusion to what was found for BD +60 1417B. Figure 8(b) shows the retrieved spectra for W0047 for the Lavie thermal profile. The retrieved spectrum generally traces the observed spectra and has a better fit to the CO feature in the *K* band and does not fit the flux peaks of the triangular *H*-band region as with BD+60 1417B. Similar to the five-point spline profile, the Mollière thermal profile retrieved spectra underestimates and poorly fits the flux in the *H* and *K* bands.

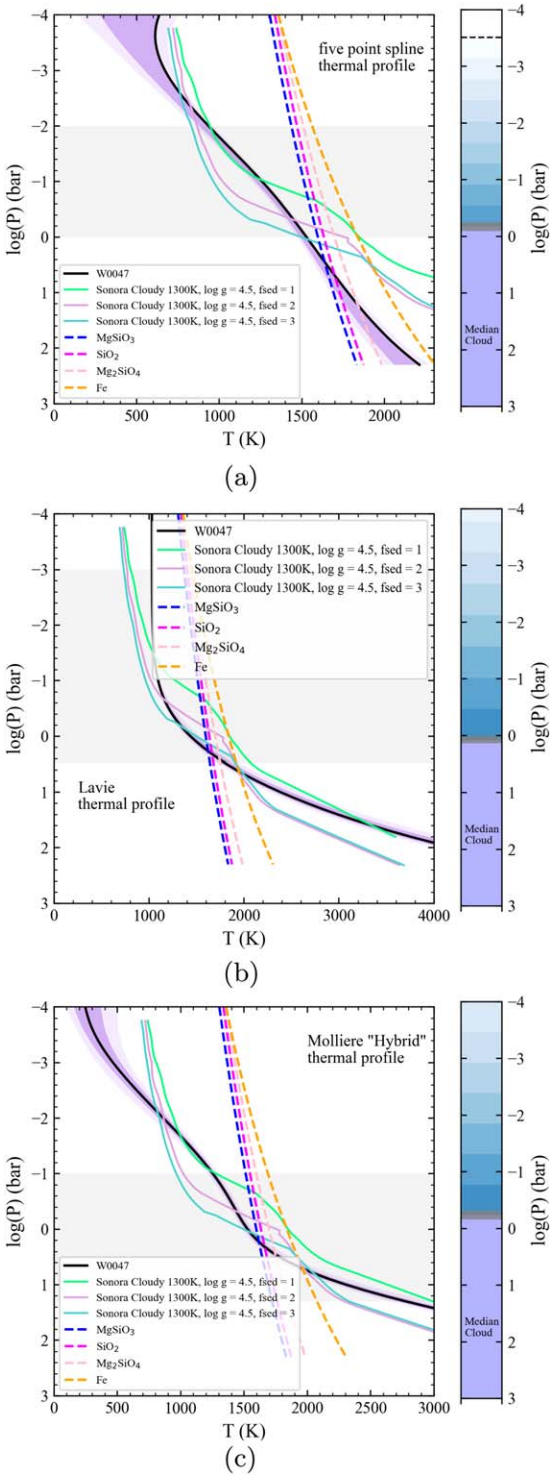

Figure 7. Retrieved thermal profile (black line, light purple shading for 1σ and 2σ intervals) and cloud pressure for W0047 for a power-law cloud deck for the Lavie thermal profile. Dashed lines show the condensation curves for possible cloud species. The light gray region is the approximate photosphere. Self-consistent grid models from Sonora Diamondback profiles for the SED-derived temperature are shown as solid colored lines (Morley et al. 2024). The median pressures of the extent of the cloud is shown in purple shading, with gray shading indicating the 1σ range, and blue shading showing the vertical distribution of the deck cloud over which the optical depth drops to 0.5. (a) W0047 thermal profiles for five-point spline, (b) Lavie profile, (c) Mollière "Hybrid" profile.

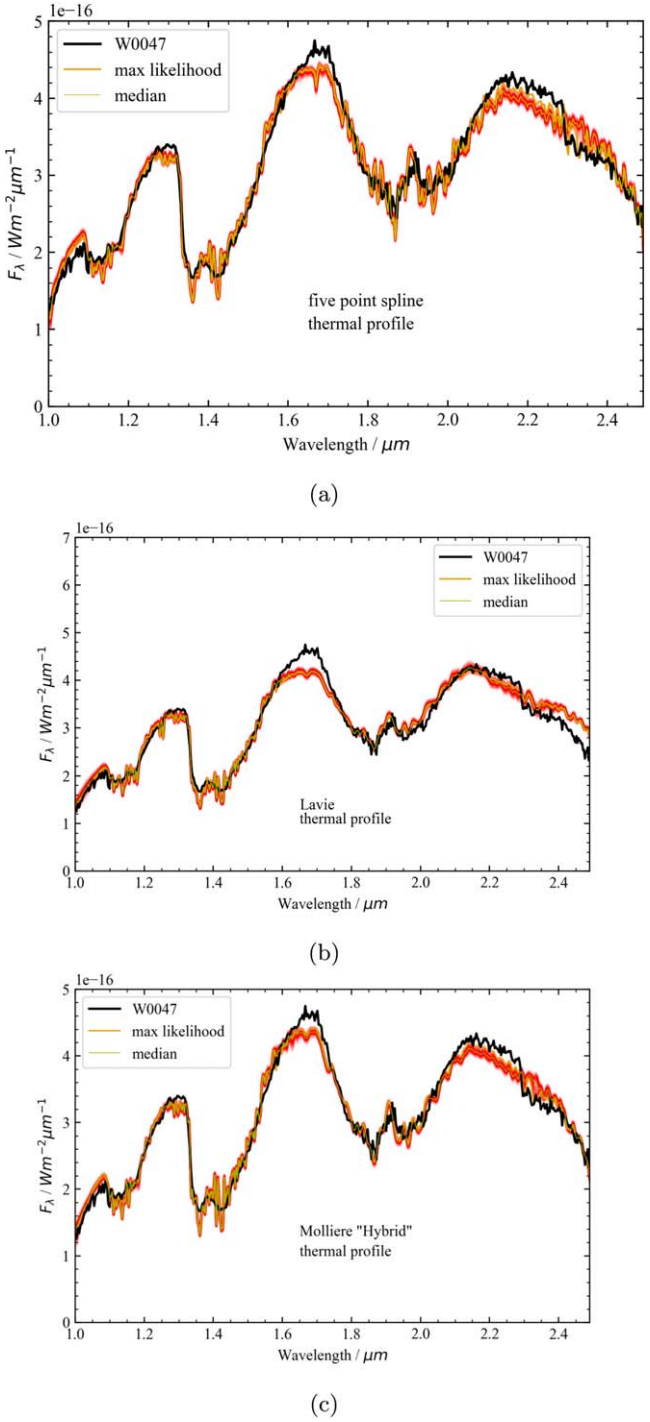

Figure 8. Retrieved forward-model spectra for the power-law deck models for W0047. The maximum-likelihood spectrum is shown in orange and the median spectrum in green. The SpeX prism data are shown in black. (a) W0047 retrieved spectra for the five-point spline thermal profile, (b) Lavie profile, (c) Mollière "Hybrid" profile.

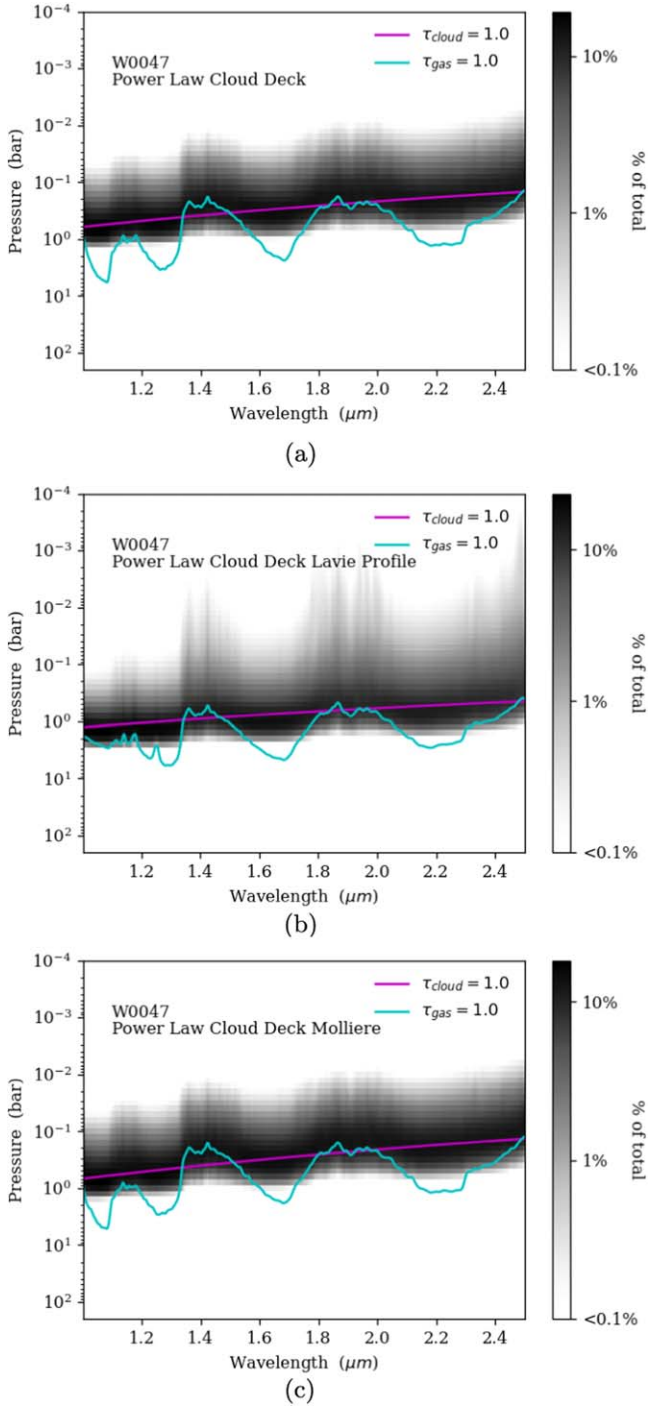

Figure 9. Contribution functions for W0047 based on the top-ranked model for each thermal parameterization cases. The black shading shows the percentage contribution of each pressure to the flux at each wavelength. $\tau = 1$ lines are included for gas-phase opacities (cyan), and a cloud (magenta). (a) W0047 contribution function for five-point spline thermal profile, (b) Lavie profile, (c) Mollière "Hybrid" profile.

For all three thermal parameterizations, the retrieved spectra underestimates the flux peak in the *J* band.

Figure 9 shows the contribution functions for W0047 for the winning cloud deck power-law models. For the five-point spline thermal profile, the bulk of the flux between $\approx 10^{-2}$ and 1 bar contributes to the observed spectrum. Across the spectrum for the five-point spline thermal profile (Figure 9(a)), the cloud opacity dominates, except for the $\approx$1.4 μm region, where H_2O opacity contributes significantly. For the Lavie thermal profile, the bulk of the flux between $\approx$0.003 and 10 bars contributes to the observed spectrum. The cloud opacity has a large contribution across the full spectrum, with the exception of a small region in the *H* band ($\approx$1.8–2.0 μm), where gas opacity becomes more important. Notably, the observable photosphere extends to the lowest pressures of the three thermal parameterizations that were tested.

For the Mollière thermal profile, the cloud opacity dominates the spectrum except for the ≈1.4 μm region, where the gas opacity is dominant. The contribution function for the Mollière thermal profile is similar to that of the five-point spline, where the bulk of the flux between $\approx 10^{-2}$ and 1 bar contributes to the observed spectrum.

9.4. Retrieved Gas Abundances and Fundamental Parameters

Figure 10 shows the retrieved gas mixing ratios compared to predictions from thermochemical equilibrium models for W0047. As before, the thermochemical equilibrium models are calculated and interpolated for our derived metallicity and C/O ratio for the three thermal profile parameterizations. In the cases where the C/O ratio cannot be determined (due to implausibly high abundances), we assume solar values (Asplund et al. 2009).

For the five-point spline thermal model (Figure 10(a)), the thermochemical equilibrium models predict many of the included gases to remain relatively constant with altitude (e.g., H_2O, CO, CO_2, and Na+K) in the photosphere. However, FeH and CrH are predicted to vary within the photosphere (denoted by the gray box). As with the retrieved abundances for BD+60 1417B for the five-point spline, we retrieve an implausibly high H_2O abundance that does not match thermochemical equilibrium predictions. Similarly, our retrieved CO abundance is depleted compared to predicted values. In Figure B2, we show the posterior distribution for retrieved and derived parameters for W0047.

We show the retrieved gas mixing ratios compared to the thermochemical equilibrium abundances for the Lavie profile (Figure 10(b)). For this thermal profile parameterization, the retrieved abundances are more constrained compared to the five-point spline and Mollière thermal profiles. However, none of the retrieved abundances match the predicted thermochemical equilibrium abundances.

Similar to the five-point spline thermal profile, for the Mollière "Hybrid" profile retrieved abundance (Figure 10(c)) we find an implausibly high H_2O abundance with respect to the predicted abundances assuming solar composition. While not a tight constraint, our CO abundance 1σ values are within the limits of the model values. FeH and CrH are predicted to vary with altitude, and show agreement with the retrieved values near the 10 bar region. Our retrieved Na+K values are not within the predicted range within the photosphere.

9.5. Cloud Properties

We find that the spectrum for W0047 is best described by a cloudy model regardless of thermal profile parameterization. A summary of cloud parameters for W0047 is shown in Table 7. The α parameter is positive for the power law, with the lowest α present for the Lavie profile.

The pressure of the cloud in the atmosphere of W0047 is shown in various shaded regions to the right of Figure 7. A notable difference is that the pressure at which $\tau > 1$ for the Lavie profile is higher than those for the five-point spline and Mollière "Hybrid" thermal profiles, indicating a higher-altitude cloud and shallower pressure of the corresponding contribution function (Figure 9(b)).

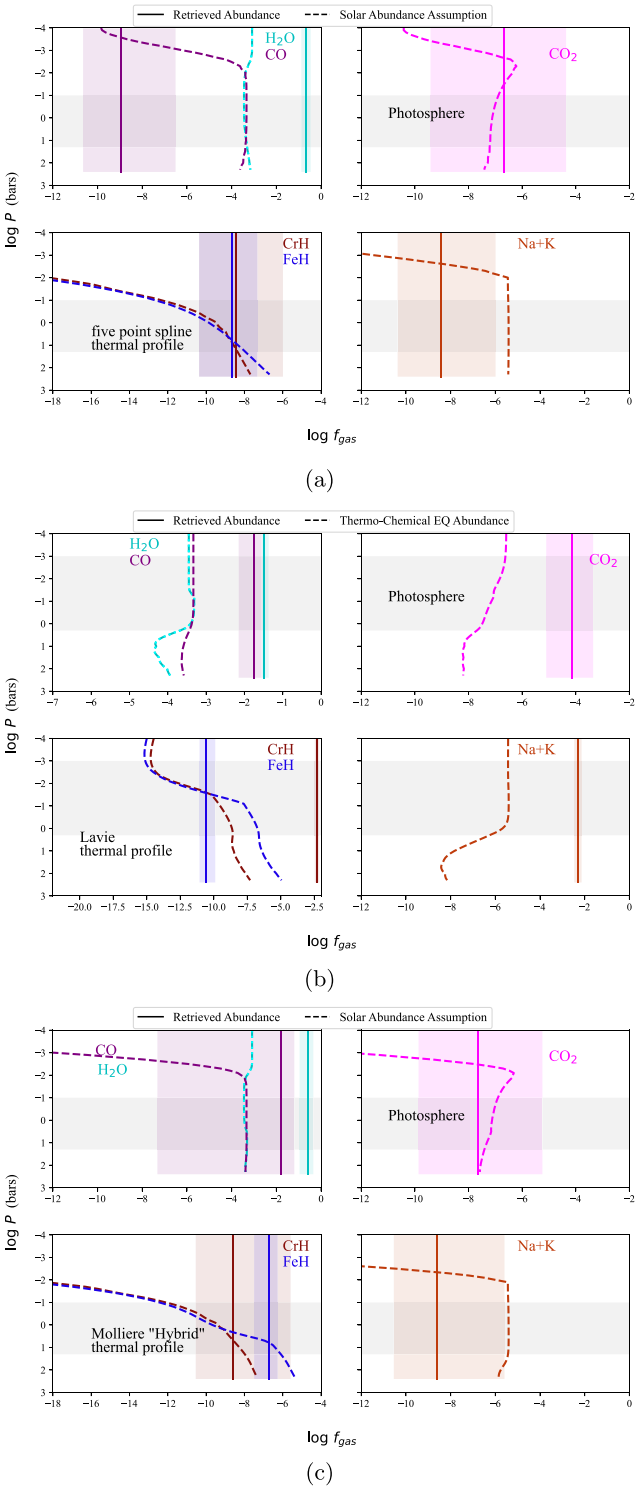

Figure 10. Retrieved uniform with altitude mixing abundances as compared to thermochemical equilibrium grid abundances for W0047. Equilibrium predictions are shown as dashed lines. The solid straight lines and shading show our median retrieved values and 16th to 84th percentiles, respectively. (a) Five-point spline thermal profile, (b) Lavie profile, (c) Mollière "Hybrid" profile.

10. Discussion

10.1. The Complexity of Low-surface-gravity L Dwarfs

Young L dwarfs are redder at near-infrared wavelengths than field objects (Faherty et al. 2013a, 2016), in part due to physical conditions brought on by a lower surface gravity.

High-altitude silicate clouds as a result of inefficient dust settling is a likely cause for low-surface-gravity object reddening (Looper et al. 2008; Suárez & Metchev 2022, 2023). The atmospheric physics and chemistry of low-surface-gravity L dwarfs brings about changes to the features and near-infrared spectral shapes that can complicate modeling and analysis (Bonnefoy et al. 2013; GRAVITY Collaboration et al. 2020; Whiteford et al. 2023).

Complexities in the retrievals of young L dwarfs like those seen within this work probably arise from compounding factors involving the emergence of condensate clouds. As noted by Rowland et al. (2023), there exist three main challenges in the near-infrared modeling of L dwarfs: (1) the limited range of the atmosphere that the near-infrared region can probe, which can limit our ability to constrain thermal profiles; (2) the different opacity sources and absorbers, which prefer uniform or nonuniform with altitude abundances; and (3) the presence of clouds that can cause degeneracies with thermal profiles.

Notably, Burningham et al. (2021) found that chemical disequilibrium and nonsolar elemental abundances are needed to accurately capture the complexity of cloudy L dwarfs in future cloud models for retrievals. Related to this regime for the directly imaged planets in the HR 8799 system, Lavie et al. (2017) commented that their future retrieval studies could also provide opportunities to explore disequilibrium chemistry through vertical mixing as well.

One clear conclusion from this work is that, regardless of the *P–T* profile chosen, both BD+60 1417B and W0047 retrieval approaches strongly preferred the cloudy model. However, what was not clear was the parameterization of said cloud with the data on hand. It remains unclear how the interplay of clouds, equilibrium chemistry, and gravity-sensitive features impacts the spectra for red young L dwarfs. Similarly, it is unclear whether the full physical picture of all those parameters is fully represented within the Brewster retrieval framework. Hence, performing the retrieval and achieving a physical or nonphysical thermal profile and abundance output is itself a test on whether we have included the full range of needed physics in order to model these complex objects.

10.2. "Free Retrievals" versus Chemical-equilibrium Assumption

Due to consistent, implausibly high abundances retrieved for BD+60 1417B and W0047, we test our retrievals assuming thermochemical equilibrium, which has previously been demonstrated by Burningham et al. (2021) and Gonzales et al. (2022). Instead of retrieving individual abundances, this method retrieves [M/H] and C/O. For simplicity, we test the chemical-equilibrium assumption on the "winning" model for the Mollière "Hybrid" profile for BD+60 1417B.

In this model, we find the following parameters: $[M/H] = 1.83^{+0.10}_{-0.16}$, $C/O = 0.38^{+0.16}_{-0.09}$, $R_{\rm Jup} = 0.51 \pm 0.01$, and $M_{\rm Jup} = 49.66^{+16.78}_{-16.79}$. The chemical-eequilibrium assumption yields a smaller radius and higher mass than with our free retrieval. While the C/O and [M/H] might be more realistic under these assumptions, our models prefer the free-retrieval assumption over the chemical-equilibrium assumption (Δlog Ev = 0 and 6.74, respectively). These results are consistent with Burningham et al. (2021), who also found that free retrievals were preferred for a higher-gravity, cloudy L dwarf.

For the chemical-equilibrium test (Figure A1(a)), we find that the retrieved *P–T* profile is not isothermal in the photosphere, unlike the "free" retrieval runs. In the photosphere, the retrieved *P–T* profile closely traces the grid model with $f_{\rm sed} = 2$. The 1σ median cloud is within the observable photosphere. Notably, we find that the chemical-equilibrium model provides a better fit to the *K*-band region containing the CO band head.

We find that while the chemical-equilibrium model does not provide a statistically better fit (Δlog Ev) for BD+60 1417B, it does provide a more plausible thermal profile. As we find that the chemical-equilibrium model (which allows abundances to vary, but in a fixed way) improves certain aspects of the retrieval, incorporating vertically varying abundances into free retrievals with Brewster may prove to be a promising next step to take (Rowland et al. 2023).

10.3. Comparison with SED-derived Fundamental Parameters

We find discrepancies for the fundamental parameters derived and extrapolated for both BD+60 1417B and W0047 regardless of thermal model parameterization compared to our SED-derived values. Our retrieved radii for BD+60 1417B and W0047 suffer from the "small-radius problem" known to be present in retrieval analysis for L and L/T transition objects (Gonzales et al. 2020, 2021, 2022; Kitzmann et al. 2020; Mollière et al. 2020; Burningham et al. 2021; Lueber et al. 2022; Vos et al. 2023). The retrieved radii for W0047 were consistently $\sim$0.5 $R_{\rm Jup}$ regardless of the thermal profile parameterization used. For BD+60 1417B, the Mollière "Hybrid" profile has an upper limit of 0.86 $R_{\rm Jup}$, the highest of the derived radii, but still inconsistent with the SED semi-empirical evolutionary model of 1.29 ± 0.06 $R_{\rm Jup}$. The high surface gravity for both BD+60 1417B and W0047 is likely driven by the unrealistically small radii. The "small radii" problem is predominantly seen in L dwarfs, therefore it may be linked to poorly parameterized cloud properties given that condensates are a dominating and difficult to model component of their spectra. The high surface gravity is persistent regardless of the thermal profile tested—also likely due to degeneracies between radius and surface gravity or a known issue with metallicity as discussed in Gonzales et al. (2021).

Across the board of thermal parameterizations, the retrieved mass for BD+60 1417B is larger than the SED semi-empirical analysis (13.47 ± 5.3 $M_{\rm Jup}$). The Mollière "Hybrid" profile produced the lowest mass of ($36.54^{+13.94}_{-12.61}$ $M_{\rm Jup}$); however, this is more than 5σ larger than the SED-derived mass. A similar observance is found for W0047. This is likely due to the small-radius problem driving a large surface gravity and in turn forcing a larger mass.

Our derived $T_{\rm eff}$ is consistently lower than the SED-derived values for both BD+60 1417B and W0047. Typically, the small-radius problem tends to push $T_{\rm eff}$ higher—whereas we see lower $T_{\rm eff}$ in both BD+60 1417B and W0047. Our low luminosity could be due to our high retrieved H_2O abundance, which in turn could be blocking flux for both BD+60 1417B and W0047.

10.4. Host-star Chemistry Implications on the Secondary

Recently, Calamari et al. (2024) introduced a theoretical chemical framework to predict cloud conditions of brown dwarfs based on FGK host stars' chemical abundances. Using the approach of Calamari et al. (2024), we utilized the chemical abundances of the host star BD+60 1417 discussed in Section 5

in order to assess the likely cloud composition of BD+60 1417B. Compared to other stars in the local solar neighborhood (e.g., Brewer et al. 2016), we find that BD+60 1417 has a relatively high Mg/Si ratio and a subsolar C/O ratio. The implications of this chemistry would be on the distribution of refractory elements into particular cloud phases (i.e., enstatite, forsterite, or quartz) and the percentage of oxygen into such silicate clouds. According to Calamari et al. (2024), using the BD+60 1417 elemental abundances of Mg, Si, C, and O, we anticipate the formation of forsterite (Mg_2SiO_4) and enstatite ($MgSiO_3$) clouds in the atmosphere of the companion. If this companion is indeed relatively silicon depleted, we would not expect a best-fit model containing a quartz cloud. As is shown in Burningham et al. (2021) and Vos et al. (2023), we also expect to see a large portion of the Fe inventory to condense as a patchy Fe deck cloud under the silicate cloud layer. Additionally, based on our host-star chemistry, we can estimate the percentage of oxygen sunk into these silicate clouds as done in Calamari et al. (2024). For this metal-rich system, we calculate an oxygen sink percentage of approximately 24%, which lies on the higher end of the local neighborhood distribution shown in Figure 2 in Calamari et al. (2024). In future modeling, we would expect this to have implications on retrieved versus bulk C/O ratio.

Finally, based on the results of Suárez & Metchev (2022), we may also expect to see more enstatite than forsterite given that this source is also a low-gravity, late-type L dwarf. Consequently, a longer-wavelength spectrum such as that enabled by JWST's MIRI spectrograph would yield strong insights into the atmosphere and ties to the host star's composition.

10.5. Predictions for the Mid-infrared Region

With a limited number of planetary-mass worlds observed with JWST (Miles et al. 2023), we have learned a wealth of information from their extended mid-infrared coverage, enabled by the MIRI spectrograph. In an effort to understand the mid-infrared region, we utilize the best-fit retrieved spectra from our three thermal profiles for both BD+60 1417B and W0047 (Figures 5 and 8, respectively) to produce extended spectra predictions from 1 to 20 μm. As stated, while we cannot constrain abundances with confidence in this work, we strongly predict the presence of clouds in both objects. We take the parameters for the maximum likelihood in each best-fit retrieval for a given *P–T* profile and rerun our forward model using the parameters over a wider wavelength range. The extrapolated spectra for BD+60 1417B and W0047 are shown in Figure 11 and serve as predictive power for what might be seen in a JWST MIRI spectrum.

We examine the extended retrieved spectrum relative to available photometric points for each source to compare/contrast the best *P–T* profile predictions. In the case of BD+60 1417B, we find that for both the five-point spline and the Mollière "Hybrid" profiles, the predicted extended spectra underestimate the flux from the WISE photometry measurements. The extrapolated spectrum for the Lavie profile most closely traces the WISE photometry, particularly at the W2 photometric point. For W0047, we find that the extracted spectra again underestimate the flux from WISE photometry measurements for both the five-point spline and Mollière "Hybrid" profiles. In contrast, the Lavie profile extracted spectrum appears to slightly overestimate the flux compared to the WISE photometry, with the exception of the W1 photometric point. While no single thermal profile prediction appears to match current data, it is clear that the JWST MIRI spectrum has the potential to differentiate the *P–T* profile and parameterize cloud properties.

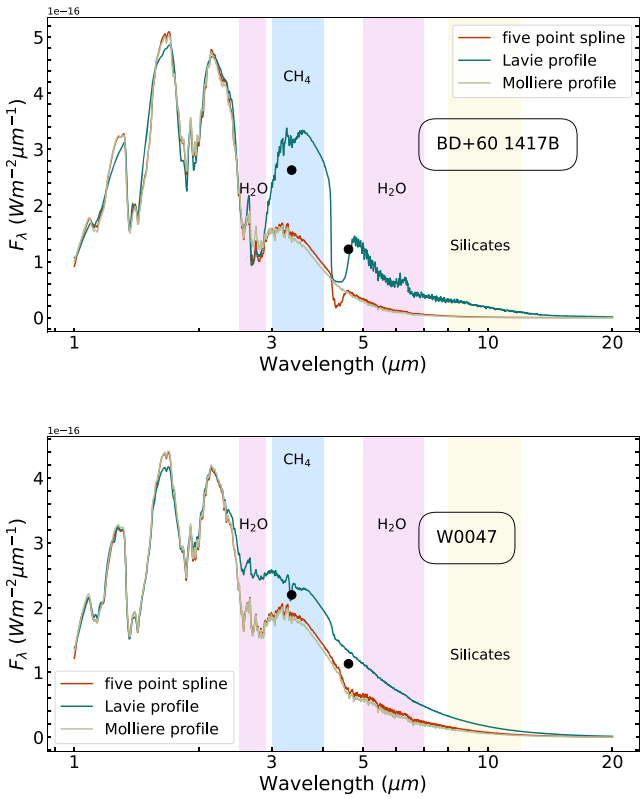

Figure 11. Extracted mid-infrared spectra for BD+60 1417B and W0047 with important molecular gases highlighted.

11. Summary and Conclusion

In this work, we present an atmospheric retrieval analysis of two young red L dwarfs with similar spectral morphology and fundamental parameters, BD+60 1417B and W0047, using the Brewster retrieval framework. We also present abundances for the K0 host star, BD+60 1417, from high-resolution spectroscopy from PEPSI/LBT (Section 5).

With the PEPSI data, we constrain an Fe abundance of 0.27 ± 0.03 dex. We constrain measurements of the C/O = 0.23 ± 0.12 and Mg/Si = 1.41 ± 0.19. Given these parameters, we find that forsterite and enstatite clouds are expected to form and not quartz clouds.

In our retrieval analysis, we test a number of different models and thermal parameterizations (five-point spline, Lavie profile, and a Mollière "Hybrid" profile) and find that both BD +60 1417B and W0047 are best described by a cloudy atmosphere regardless of the chosen *P–T* profile. Regardless of thermal profile parameterization, the retrieved profile was generally not in agreement with forward models for both BD +60 1417B and W0047. We find that for both BD+60 1417B and W0047 the retrieved spectrum from Brewster had difficulty fitting the *K*-band region, which contains the temperature-sensitive CO feature.

Lastly, although we test three different thermal profile parameterizations, we find that we are unable to reliably

constrain the C/O ratio of these planetary-mass objects due to retrieving implausibly high abundances (e.g., H_2O). Generally, we find that our abundances are not in agreement with thermochemical equilibrium models. While we experience challenges in modeling these young, low-gravity objects, we find that improvements can be made in terms of modeling approach as we discover that nonuniform with altitude abundances provide a more realistic thermal profile for BD +60 1417B. This work continues to provide technical lessons in retrieval analysis of young cloudy L dwarfs.

JWST has the capabilities to provide wider wavelength coverage and simultaneous higher-resolution and higher-signal-to-noise observations. Wide wavelength coverage will allow us to probe the *P–T* profile from (0.1–1 bar) through mid-infrared all the way to 10 bar pressure with near-infrared coverage. Near-infrared and mid-infrared data are crucial to retrieve a reliable *P–T* profile for early-to-mid L dwarfs (Burningham et al. 2021; Rowland et al. 2023; Vos et al. 2023). Future retrievals of BD+60 1417B and W0047 with JWST data would allow us to accurately constrain the *P–T* profile and cloud parameters to break degeneracies between clouds and composition.

Acknowledgments

This research has made use of the NASA Exoplanet Archive, which is operated by the California Institute of Technology, under contract with the National Aeronautics and Space Administration under the Exoplanet Exploration Program.

NASA's Astrophysics Data System Bibliographic Services together with the VizieR catalog access tool and SIMBAD database operated at CDS, Strasbourg, France, were invaluable resources for this work. This publication makes use of data products from the Two Micron All Sky Survey, which is a joint project of the University of Massachusetts and the Infrared Processing and Analysis Center/California Institute of Technology, funded by the National Aeronautics and Space Administration and the National Science Foundation.

This work benefited from involvement in ExoExplorers, which is sponsored by the Exoplanets Program Analysis Group (ExoPAG) and NASA's Exoplanet Exploration Program Office (ExEP). C.P. thanks the LSSTC Data Science Fellowship Program, which is funded by LSSTC, NSF Cybertraining grant No. 1829740, the Brinson Foundation, and the Moore Foundation; her participation in the program has benefited this work. E.J.G. is supported by an NSF Astronomy and Astrophysics Postdoctoral Fellowship under award AST-2202135. E.G. acknowledges support from the Heising-Simons Foundation for this research. J.M.V. acknowledges support from a Royal Society—Science Foundation Ireland University Research Fellowship (grant No. URF\1\221932). B.B. acknowledges support from UK Research and Innovation Science and Technology Facilities Council (grant No. ST/X001091/1).

This work benefited from the 2023 Exoplanet Summer Program in the Other Worlds Laboratory (OWL) at the University of California, Santa Cruz, a program funded by the Heising-Simons Foundation and NASA.

This work is supported by the National Science Foundation under grant No. 2143400.

This work has made use of data from the European Space Agency (ESA) mission Gaia (https://www.cosmos.esa.int/gaia), processed by Gaia. This publication makes use of data products from the Wide-field Infrared Survey Explorer, which is a joint project of the University of California, Los Angeles, and the Jet Propulsion Laboratory/California Institute of Technology, funded by the National Aeronautics and Space Administration. Data Processing and Analysis Consortium (DPAC; https://www.cosmos.esa.int/web/gaia/dpac/consortium). Funding for the DPAC has been provided by national institutions, in particular the institutions participating in the Gaia Multilateral Agreement.

This work is based on observations made with the Large Binocular Telescope. The LBT is an international collaboration among institutions in the United States, Italy, and Germany. The LBT Corporation partners are The University of Arizona on behalf of the Arizona Board of Regents; Istituto Nazionale di Astrofisica, Italy; LBT Beteiligungsgesellschaft, Germany, representing the Max-Planck Society, The Leibniz Institute for Astrophysics Potsdam, and Heidelberg University; and The Ohio State University, representing OSU, University of Notre Dame, University of Minnesota, and University of Virginia.

The data used in this publication were collected through the MENDEL high-performance computing (HPC) cluster at the American Museum of Natural History. This HPC cluster was developed with National Science Foundation (NSF) Campus Cyberinfrastructure support through Award 1925590. This work was also supported by the National Science Foundation via awards 1909776, 1614527, and AST-1909837.

Computation reported in this work was also carried out on the Unity cluster of the College of Arts and Sciences at the Ohio State University. The computational resources and support provided are gratefully acknowledged.

Facilities: Exoplanet Archive, LBT (PEPSI).

Software: `Brewster` (Burningham et al. 2017), `PyMultiNest` (Buchner et al. 2014), `corner.py` (Foreman-Mackey et al. 2013).

Appendix A
Chemical-equilibrium Assumption Model

In Figure A1, we present the retrieval plots for the chemical-equilibrium test for the winning Mollière "Hybrid" profile for BD+60 1417B. While this model is not preferred over the free retrieval, we discuss the implications of testing this retrieval setup.

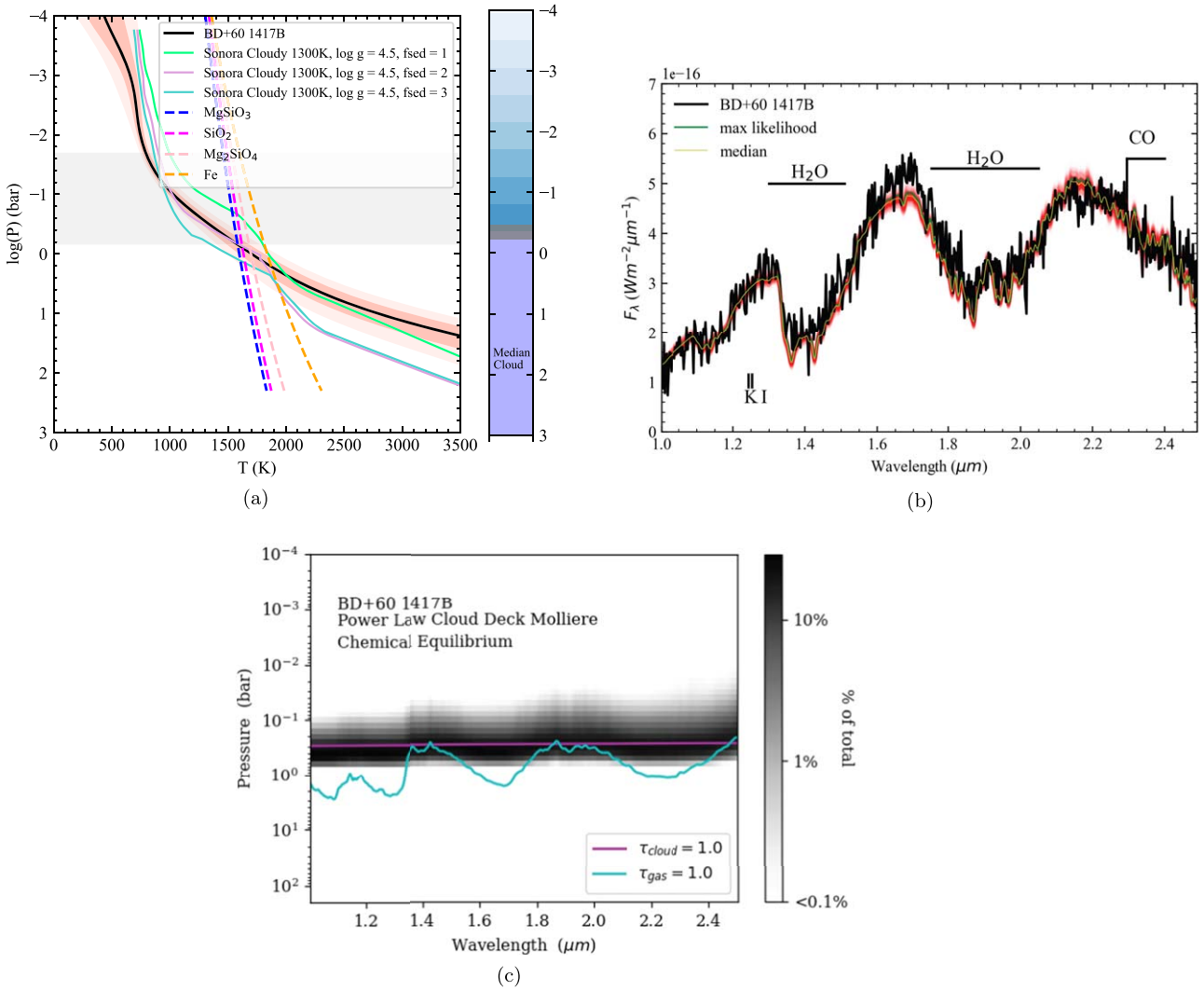

Figure A1. (a) Retrieved thermal profile for the winning Mollière "Hybrid" profile for BD+60 1417B under the assumption of chemical equilibrium. (b) Retrieved forward-model spectra for BD+60 1417B for chemical equilibrium. (c) Contribution function for BD+60 1417B for the winning model.

Appendix B
Corner Plots

In Figures B1 and B2, we present the posteriors for the gas abundances and derived fundamental parameters for the three different thermal profile parameterizations used in our retrievals for BD+60 1417B and W0047, respectively.

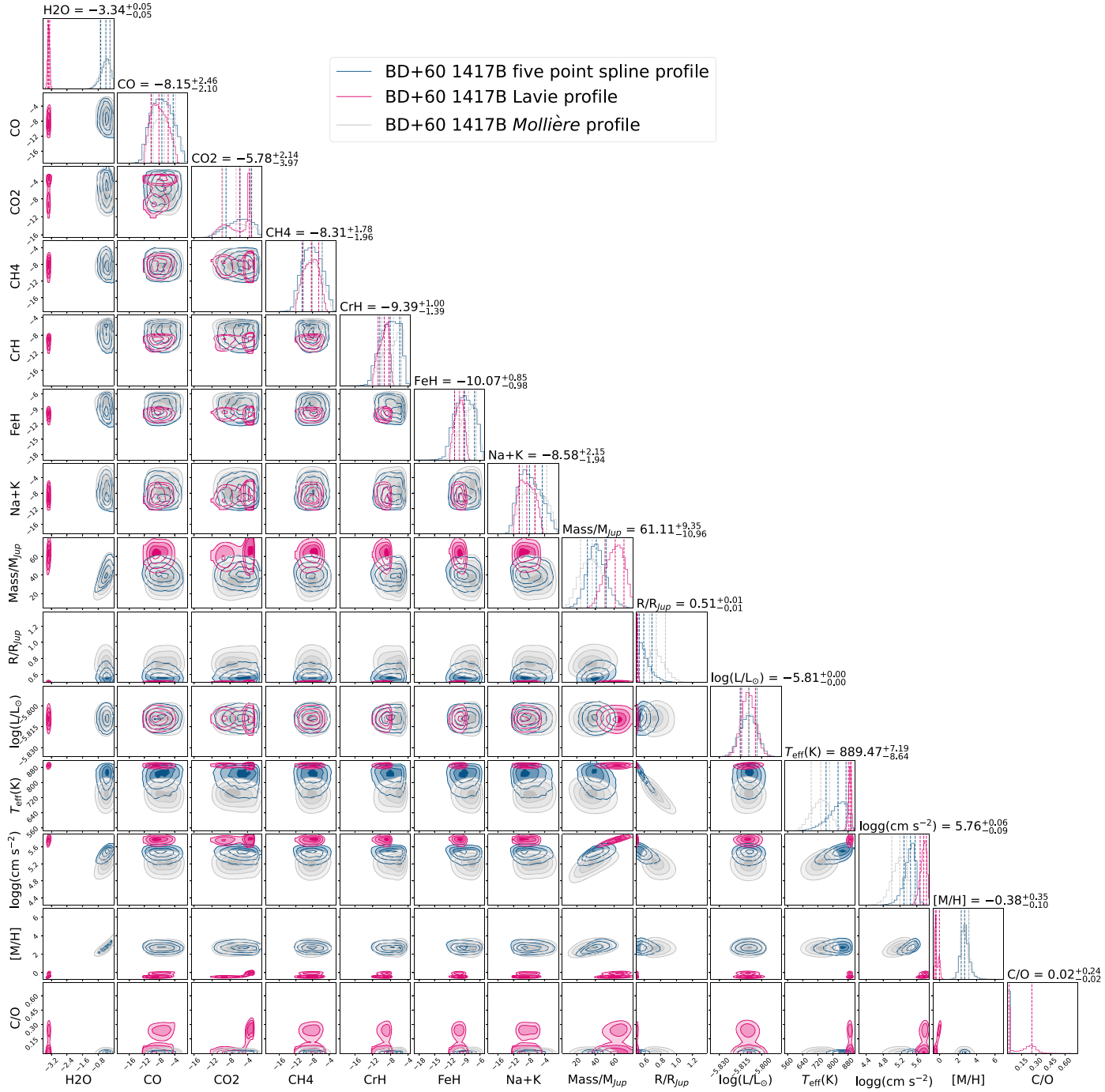

Figure B1. Best-fit models for the five-point spline thermal profile, Lavie profile, and Mollière profile for BD+60 1417B: power-law cloud deck (blue), gray cloud deck (pink), and power-law cloud deck (silver) for best fits, respectively. Posterior probability distributions for retrieved gas abundances, mass, radius, and derived quantities of the best-fit models. Far-right diagonal plots show marginalized posteriors for each parameter along with 2D parameter correlation histograms. Dashed lines show the median retrieved value (reported value) along with 1σ confidence intervals. Gas abundances are in units of dex.

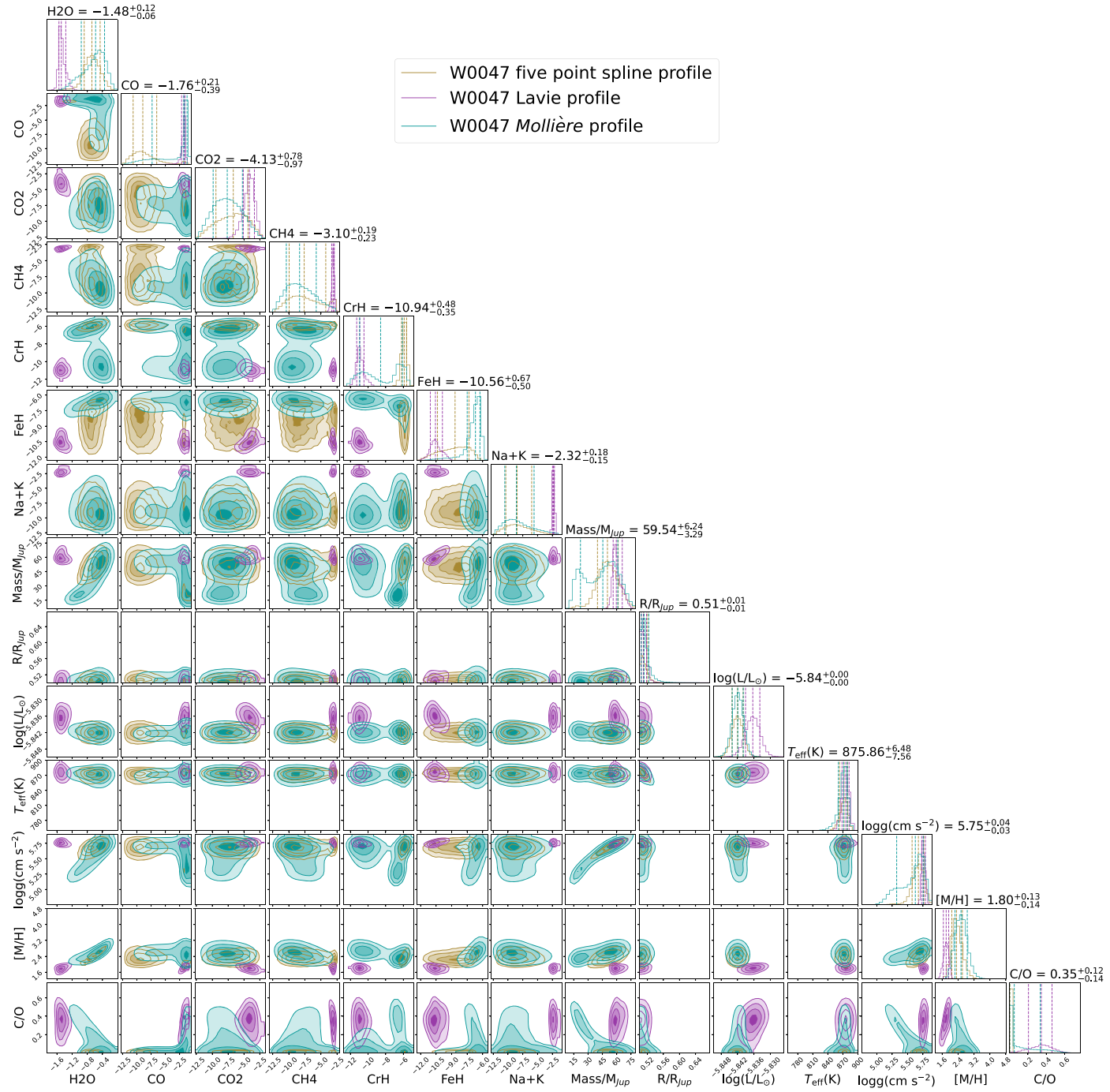

Figure B2. Best-fit models for the five-point spline thermal profile, Lavie profile, and Mollière profile for W0047: power-law cloud deck (gold), power-law cloud deck (purple), and power-law cloud deck (green) for best fits, respectively. Posterior probability distributions for retrieved gas abundances, mass, radius, and derived quantities of the best-fit models. Far-right diagonal plots show marginalized posteriors for each parameter along with 2D parameter correlation histograms. Dashed lines show the median retrieved value (reported value) along with 1σ confidence intervals. Gas abundances are in units of dex.

ORCID iDs

Caprice L. Phillips https://orcid.org/0000-0001-5610-5328
Jacqueline K. Faherty https://orcid.org/0000-0001-6251-0573
Ben Burningham https://orcid.org/0000-0003-4600-5627
Johanna M. Vos https://orcid.org/0000-0003-0489-1528
Eileen C. Gonzales https://orcid.org/0000-0003-4636-6676
Emily J. Griffith https://orcid.org/0000-0001-9345-9977
Sherelyn Alejandro Merchan https://orcid.org/0000-0003-0548-0093
Emily Calamari https://orcid.org/0000-0002-2682-0790
Channon Visscher https://orcid.org/0000-0001-6627-6067
Caroline V. Morley https://orcid.org/0000-0002-4404-0456
Niall Whiteford https://orcid.org/0000-0001-8818-1544
Ilya Ilyin https://orcid.org/0000-0002-0551-046X
Klaus Strassmeier https://orcid.org/0000-0002-6192-6494
Ji Wang https://orcid.org/0000-0002-4361-8885

References

Asplund, M., Grevesse, N., Sauval, A. J., & Scott, P. 2009, ARA&A, 47, 481
Bate, M. R., Bonnell, I. A., & Bromm, V. 2002, MNRAS, 332, L65
Bell, K. L. 1980, JPhB, 13, 1859
Bell, K. L., & Berrington, K. A. 1987, JPhB, 20, 801
Bergemann, M., Collet, R., Amarsi, A. M., et al. 2017, ApJ, 847, 15
Bergemann, M., Hoppe, R., Semenova, E., et al. 2021, MNRAS, 508, 2236
Bergemann, M., Kudritzki, R.-P., Würl, M., et al. 2013, ApJ, 764, 115
Blanco-Cuaresma, S. 2019, MNRAS, 486, 2075
Blanco-Cuaresma, S., Soubiran, C., Heiter, U., & Jofré, P. 2014, A&A, 569, A111
Bonnefoy, M., Boccaletti, A., Lagrange, A. M., et al. 2013, A&A, 555, A107
Bonnell, I. A., Clark, P., & Bate, M. R. 2008, MNRAS, 389, 1556
Brewer, J. M., Fischer, D. A., Valenti, J. A., & Piskunov, N. 2016, ApJS, 225, 32
Buchner, J., Georgakakis, A., Nandra, K., et al. 2014, A&A, 564, A125
Buder, S., Sharma, S., Kos, J., et al. 2021, MNRAS, 506, 150
Burgasser, A. 2010, in Exoplanets Rising: Astronomy and Planetary Science at the Crossroads, 24
Burningham, B., Faherty, J. K., Gonzales, E. C., et al. 2021, MNRAS, 506, 1944
Burningham, B., Marley, M. S., Line, M. R., et al. 2017, MNRAS, 470, 1177
Burrows, A., Heng, K., & Nampaisarn, T. 2011, ApJ, 736, 47
Calamari, E., Faherty, J. K., Burningham, B., et al. 2022, ApJ, 940, 164
Calamari, E., Faherty, J. K., Visscher, C., et al. 2024, ApJ, 963, 67
Chilcote, J., Pueyo, L., De Rosa, R. J., et al. 2017, AJ, 153, 182
Cutri, R. M., Skrutskie, M. F., van Dyk, S., et al. 2003, 2MASS All Sky Catalog of Point Sources (Washington, DC: NASA)
Cutri, R. M., et al. 2012, Explanatory Supplement to the WISE All-Sky Data Release Products
Faherty, J. K., Cruz, K. L., Rice, E. L., & Riedel, A. 2013a, MmSAI, 84, 955
Faherty, J. K., Gagné, J., Popinchalk, M., et al. 2021, ApJ, 923, 48
Faherty, J. K., Rice, E. L., Cruz, K. L., Mamajek, E. E., & Núñez, A. 2013b, AJ, 145, 2
Faherty, J. K., Riedel, A. R., Cruz, K. L., et al. 2016, ApJS, 225, 10
Filippazzo, J. 2020, SEDkit: Spectral Energy Distribution Construction and Analysis Tools, Astrophysics Source Code Library, ascl:2011.014
Filippazzo, J. C., Rice, E. L., Faherty, J., et al. 2015, ApJ, 810, 158
Foreman-Mackey, D., Hogg, D. W., Lang, D., & Goodman, J. 2013, PASP, 125, 306
Freedman, R. S., Lustig-Yaeger, J., Fortney, J. J., et al. 2014, ApJS, 214, 25
Freedman, R. S., Marley, M. S., & Lodders, K. 2008, ApJS, 174, 504
Fulbright, J. P. 2000, AJ, 120, 1841
Gaarn, J., Burningham, B., Faherty, J. K., et al. 2023, MNRAS, 521, 5761
Gaia Collaboration, Brown, A. G. A., Vallenari, A., et al. 2021, A&A, 649, A1
Gaia Collaboration, Vallenari, A., Brown, A. G. A., et al. 2023, A&A, 674, A1
Gilmore, G., Randich, S., Asplund, M., et al. 2012, Msngr, 147, 25
Gizis, J. E., Allers, K. N., Liu, M. C., et al. 2015, ApJ, 799, 203
Gizis, J. E., Faherty, J. K., Liu, M. C., et al. 2012, AJ, 144, 94
Gonzales, E. C., Burningham, B., Faherty, J. K., et al. 2020, ApJ, 905, 46
Gonzales, E. C., Burningham, B., Faherty, J. K., et al. 2021, ApJ, 923, 19
Gonzales, E. C., Burningham, B., Faherty, J. K., et al. 2022, ApJ, 938, 56
GRAVITY Collaboration, Nowak, M., Lacour, S., et al. 2020, A&A, 633, A110
Gustafsson, B., Edvardsson, B., Eriksson, K., et al. 2008, A&A, 486, 951
Heiter, U., Lind, K., Bergemann, M., et al. 2021, A&A, 645, A106
Heng, K., Mendonça, J. M., & Lee, J.-M. 2014, ApJS, 215, 4
Hoch, K. K. W., Konopacky, Q. M., Theissen, C. A., et al. 2023, AJ, 166, 85
Jofré, P., Heiter, U., & Soubiran, C. 2019, ARA&A, 57, 571
John, T. L. 1988, A&A, 193, 189
Kass, R. E., & Raftery, A. E. 1995, JASA, 90, 773
Kirkpatrick, J. D. 2005, ARA&A, 43, 195
Kitzmann, D., Heng, K., Oreshenko, M., et al. 2020, ApJ, 890, 174
Konopacky, Q. M., Barman, T. S., Macintosh, B. A., & Marois, C. 2013, Sci, 339, 1398
Kumar, S. S. 1963, ApJ, 137, 1121
Lacy, B. I., & Burrows, A. 2020, ApJ, 904, 25
Lavie, B., Mendonça, J. M., Mordasini, C., et al. 2017, AJ, 154, 91
Lew, B. W. P., Apai, D., Zhou, Y., et al. 2016, ApJL, 829, L32
Line, M. R., Teske, J., Burningham, B., Fortney, J. J., & Marley, M. S. 2015, ApJ, 807, 183
Liu, M. C., Dupuy, T. J., & Allers, K. N. 2016, ApJ, 833, 96
Looper, D. L., Kirkpatrick, J. D., Cutri, R. M., et al. 2008, ApJ, 686, 528
Lueber, A., Kitzmann, D., Bowler, B. P., Burgasser, A. J., & Heng, K. 2022, ApJ, 930, 136
Luhman, K. L., Joergens, V., Lada, C., et al. 2007, in Protostars and Planets V, ed. B. Reipurth, D. Jewitt, & K. Keil (Tucson, AZ: Univ. Arizona Press), 443
MacDonald, R. J., & Batalha, N. E. 2023, RNAAS, 7, 54
Madhusudhan, N. 2019, ARA&A, 57, 617
Madhusudhan, N., Apai, D., & Gandhi, S. 2016, arXiv:1612.03174
Madhusudhan, N., & Seager, S. 2009, ApJ, 707, 24
Maldonado, J., & Villaver, E. 2017, A&A, 602, A38
Manjavacas, E., Apai, D., Zhou, Y., et al. 2019, AJ, 157, 101
Marley, M. S., Saumon, D., Cushing, M., et al. 2012, ApJ, 754, 135
Marley, M. S., Saumon, D., Guillot, T., et al. 1996, Sci, 272, 1919
Marley, M. S., Saumon, D., Visscher, C., et al. 2021, ApJ, 920, 85
Marocco, F., Eisenhardt, P. R. M., Fowler, J. W., et al. 2021, ApJS, 253, 8
Marois, C., Zuckerman, B., Konopacky, Q. M., Macintosh, B., & Barman, T. 2010, Natur, 468, 1080
Mashonkina, L., Korn, A. J., & Przybilla, N. 2007, A&A, 461, 261
McKay, C. P., Pollack, J. B., Zent, A. P., Cruikshank, D. P., & Courtin, R. 1989, GeoRL, 16, 973
Miles, B. E., Biller, B. A., Patapis, P., et al. 2023, ApJL, 946, L6
Mollière, P., Stolker, T., Lacour, S., et al. 2020, A&A, 640, A131
Moore, C. E., Minnaert, M. G. J., & Houtgast, J. 1966, The Solar Spectrum 2935 A to 8770 A (Washington, DC: USGPO)
Morley, C. V., Fortney, J. J., Marley, M. S., et al. 2012, ApJ, 756, 172
Morley, C. V., Mukherjee, S., Marley, M. S., et al. 2024, arXiv:2402.00758
Mucciarelli, A., Pancino, E., Lovisi, L., Ferraro, F. R., & Lapenna, E. 2013, ApJ, 766, 78
Nakajima, T., Oppenheimer, B. R., Kulkarni, S. R., et al. 1995, Natur, 378, 463
Öberg, K. I., Murray-Clay, R., & Bergin, E. A. 2011, ApJL, 743, L16
Oppenheimer, B. R., Kulkarni, S. R., Matthews, K., & Nakajima, T. 1995, Sci, 270, 1478
Rajan, A., Rameau, J., De Rosa, R. J., et al. 2017, AJ, 154, 10
Richard, C., Gordon, I., Rothman, L., et al. 2012, JQSRT, 113, 1276
Rowland, M. J., Morley, C. V., & Line, M. R. 2023, ApJ, 947, 6
Ruffio, J.-B., Konopacky, Q. M., Barman, T., et al. 2021, AJ, 162, 290
Saumon, D., & Marley, M. S. 2008, ApJ, 689, 1327
Saumon, D., Marley, M. S., Abel, M., Frommhold, L., & Freedman, R. S. 2012, ApJ, 750, 74
Sneden, C. A. 1973, PhD thesis, Univ. of Texas, Austin
Stassun, K. G., Oelkers, R. J., Pepper, J., et al. 2018, AJ, 156, 102
Strassmeier, K. G., Ilyin, I., Järvinen, A., et al. 2015, AN, 336, 324
Strassmeier, K. G., Ilyin, I., & Steffen, M. 2018, A&A, 612, A44
Suárez, G., & Metchev, S. 2022, MNRAS, 513, 5701
Suárez, G., & Metchev, S. 2023, MNRAS, 523, 4739
Toon, O. B., McKay, C. P., Ackerman, T. P., & Santhanam, K. 1989, JGR, 94, 16287
Tremblin, P., Chabrier, G., Baraffe, I., et al. 2017, ApJ, 850, 46
Vos, J. M., Allers, K. N., Biller, B. A., et al. 2018, MNRAS, 474, 1041
Vos, J. M., Burningham, B., Faherty, J. K., et al. 2023, ApJ, 944, 138
Wang, J., Kolecki, J. R., Ruffio, J.-B., et al. 2022, AJ, 163, 189
Wang, J., Wang, J. J., Ma, B., et al. 2020, AJ, 160, 150
Wang, J., Wang, J. J., Ruffio, J.-B., et al. 2023, AJ, 165, 4
Whiteford, N., Glasse, A., Chubb, K. L., et al. 2023, MNRAS, 525, 1375
Whitworth, A. 2007, Multiplicity in Star Formation, 41
Whitworth, A. 2018, arXiv:1811.06833
Whitworth, A., Stamatellos, D., Walch, S., et al. 2010, in IAU Symp. 266, Star Clusters: Basic Galactic Building Blocks Throughout Time and Space, ed. R. de Grijs & J. R. D. Lépine (Cambridge: Cambridge Univ. Press), 264
Whitworth, A. P., & Goodwin, S. 2005, AN, 326, 899
Whitworth, A. P., & Stamatellos, D. 2006, A&A, 458, 817
Xuan, J. W., Wang, J., Ruffio, J.-B., et al. 2022, ApJ, 937, 54
Xuan, J. W., Wang, J. J., Finnerty, L., et al. 2024, ApJ, 962, 10